

Water Resources Research®



RESEARCH ARTICLE

10.1029/2022WR033445

Linking Stream Chemistry to Subsurface Redox Architecture

Andrew R. Shaughnessy¹ , Michael J. Forngeng¹ , Tao Wen² , Xin Gu^{1,3} ,
Jordon D. Hemingway⁴ , and Susan L. Brantley^{1,5} 

Key Points:

- Blind-source attribution of endmember sources of sulfate can elucidate open-versus closed-system pyrite oxidation
- Concentration-discharge relationships reflect deep and shallow pyrite oxidation in small and large watersheds, respectively
- Pyrite oxidation in watersheds with coal mining is kinetically limited, while oxidation in watersheds without mining is limited by oxygen transport

Supporting Information:

Supporting Information may be found in the online version of this article.

Correspondence to:

A. R. Shaughnessy,
and61220@gmail.com

Citation:

Shaughnessy, A. R., Forngeng, M. J., Wen, T., Gu, X., Hemingway, J. D., & Brantley, S. L. (2023). Linking stream chemistry to subsurface redox architecture. *Water Resources Research*, 59, e2022WR033445. <https://doi.org/10.1029/2022WR033445>

Received 11 AUG 2022

Accepted 11 APR 2023

Author Contributions:

Conceptualization: Andrew R. Shaughnessy, Tao Wen, Xin Gu, Susan L. Brantley
Data curation: Andrew R. Shaughnessy
Formal analysis: Andrew R. Shaughnessy, Michael J. Forngeng, Tao Wen, Xin Gu, Jordon D. Hemingway, Susan L. Brantley
Funding acquisition: Susan L. Brantley
Investigation: Andrew R. Shaughnessy, Susan L. Brantley
Methodology: Andrew R. Shaughnessy, Michael J. Forngeng, Tao Wen, Jordon D. Hemingway, Susan L. Brantley
Resources: Susan L. Brantley

¹Department of Geosciences, Pennsylvania State University, University Park, PA, USA, ²Department of Earth and Environmental Sciences, Syracuse University, Syracuse, NY, USA, ³Environmental Sciences Division, Oak Ridge National Laboratory, Oak Ridge, TN, USA, ⁴Department of Earth Sciences, Geological Institute, ETH Zurich, Zurich, Switzerland, ⁵Earth and Environmental Systems Institute, Pennsylvania State University, University Park, PA, USA

Abstract As drinking-water scarcity grows worldwide, we need to improve predictions of the quantity and quality of our water resources. An overarching problem for model improvement is that we do not know the geological structure of aquifers in sufficient detail. In this work, we demonstrate that mineral-water reactions imprint structure in the subsurface that impacts the flow and transport of some chemical species. Specifically, pyrite, a ubiquitous mineral, commonly oxidizes and depletes in the upper layers of the weathering profile in most humid watersheds, only remaining at depths of meters. We hypothesize that variations in concentrations (C) of pyrite-derived sulfate released into rivers as a function of discharge (q) reflect the rate-limiting step and depth of pyrite-oxidizing layers. We found that $\log C - \log q$ behaviors thus differ in small and large watersheds in the Susquehanna River Basin as well as in selected watersheds in the Western United States. Although coal mining changes pyrite oxidation from closed to open system with respect to O_2 , patterns in stream chemistry as a function of discharge are consistent with deep and shallow pyrite oxidation zones in small and large watersheds respectively. Therefore, understanding the subsurface patterns of mineral reactions and how they affect the architecture of aquifers will elucidate patterns of changing river chemistry and our ability to manage water resources in the future under accelerated land use and climate change.

1. Introduction

Geologists investigate the evolution of the land surface through direct observation. In contrast, below the land surface, water dissolves and precipitates minerals in localized zones called reaction fronts that define landscapes we cannot see Brantley et al. (2014). These subsurface landscapes have both a physical and chemical structure that impact many processes such as groundwater flow and storage (e.g., Hoagland et al., 2017; Molli et al., 2015; Poole et al., 2006; Xu et al., 2021) and contaminant fate and transport (e.g., Essaid et al., 2015; Kim et al., 2019; Xu et al., 2022). Of particular interest is the redox architecture of a watershed, a term we use to refer to the zones of oxidized and unoxidized deep subsurface (Gu, Rempe, et al., 2020). Understanding the redox architecture of a watershed, including both minerals and organic matter, is essential because the fate and transport of many environmental contaminants depend on redox processes along subsurface flow paths (e.g., Borch et al., 2010). For example, nitrate leaching into groundwater from excess fertilizer application is one of the major threats to environmental and public health worldwide (e.g., Galaviz-Villa et al., 2010). Although conservation efforts have reduced nitrate runoff from farms (application timescales of decades to centuries), stream nitrate concentrations have remained high due to the persistence of legacy nitrate in groundwater (groundwater residence times of centuries to millennia; Van Meter et al., 2017, 2018). Whether or not a watershed is susceptible to legacy contamination may depend in part on its underlying redox architecture (Tesoriero et al., 2013, 2015). Several studies have aimed to predict redox conditions in groundwater using measurements of redox-sensitive species (e.g., dissolved oxygen [DO]), watershed characteristics (e.g., lithology, land use, and soil properties), and statistical analysis (e.g., Botchet et al., 2020; Close et al., 2016; Friedel et al., 2020; Tesoriero et al., 2017, 2015), but interpreting these results with respect to watershed function and contaminant transport remains difficult—especially at large spatial scales—because of landscape heterogeneity.

While we do not focus on the nitrate system here, we nonetheless explore the redox architecture of the subsurface by investigating pyrite oxidation. Pyrite, a ubiquitous iron sulfide accessory mineral, is generally depleted through oxidation in the upper layers of near-surface rock through interaction with oxygenated water (Gu, Rempe, et al., 2020, and citations therein). In fact, only rarely are detrital pyrite-containing sediments found in the rock record since atmospheric oxygen levels increased above 10^{-5} PAL (present atmospheric level) because

© 2023. The Authors.

This is an open access article under the terms of the [Creative Commons Attribution License](https://creativecommons.org/licenses/by/4.0/), which permits use, distribution and reproduction in any medium, provided the original work is properly cited.

Software: Andrew R. Shaughnessy
Supervision: Susan L. Brantley
Validation: Andrew R. Shaughnessy
Visualization: Andrew R. Shaughnessy
Writing – original draft: Andrew R. Shaughnessy
Writing – review & editing: Andrew R. Shaughnessy, Michael J. Forggeng, Tao Wen, Xin Gu, Jordon D. Hemingway, Susan L. Brantley

pyrite in these particles oxidizes so rapidly near Earth's surface (Johnson et al., 2019). Gu, Rempe, et al. (2020) showed that many rocks remain unaffected by oxidation at depths of tens of meters below the land surface but are completely pyrite-free at the land surface. A depth interval of oxidation (a reaction front) somewhat parallels the land surface under many headwater catchments (e.g., Brantley et al., 2014; Gu, Heaney, et al., 2020; Wan et al., 2019). In some watersheds, where the front is sub-parallel to the land surface, pyrite-containing rock never reaches the land surface, but in other watersheds, river incision exposes pyrite in the channel (Gu, Heaney, et al., 2020). We hypothesized that the pyrite oxidation front might indicate the transition from oxic to anoxic groundwater in a watershed and might control the dynamics of sulfate concentrations in stream waters. Understanding the weathering profiles of pyrite in the subsurface (i.e., the depth of the reaction front across watersheds) might eventually enhance predictions of transport for redox-active contaminants such as nitrate or organic compounds.

Here, we join a machine learning-based mixing model with a physically based oxidation model to explore what concentration-discharge relationships can teach us about the subsurface redox architecture of a watershed across spatial scales, and we apply it to watersheds in the United States (US) using publicly accessible water quality databases. This investigation is important because, although it is known that outcropping rock type is a major control on river chemistry (e.g., Gaillardet et al., 1999; Hartmann, 2009; Meybeck, 1987), we do not typically have detailed information about the subsurface, especially at large spatial scales, and we, therefore, do not know how it affects riverine chemistries. Studies have nonetheless demonstrated how subsurface mineral distributions impact river chemistry (e.g., Torres et al., 2015; Zhi et al., 2019), with several specifically targeting sulfide mineral oxidation (e.g., Hilton et al., 2021; Kemeny et al., 2021; Wan et al., 2019; Winnick et al., 2017). If our understanding of the linkages between stream concentration and the subsurface redox architecture is improved, our ability to predict water quality and legacy contamination could greatly increase.

2. Methods

2.1. Data Acquisition

For this study, we first aggregated data sets of stream concentration and discharge measurements in a series of four increasingly larger, nested watersheds on sedimentary rock that range from first order to seventh order (HUC16 to HUC4; Figure 1; Table S3 in Supporting Information S1). For the smallest watershed known as Shale Hills (HUC16; Figure 1a), we utilized data collected from 2008 to 2010 (Brantley et al., 2013a; Brantley et al., 2013b; Brantley et al., 2013c). For the next larger watershed of Shaver's Creek (HUC10; Figure 1b), we utilized data sets from three locations for samples collected from 2014 to 2020 (Brantley et al., 2018a; Brantley, Forsythe, Hoagland, Pederson, & Russo, 2018, this study). This HUC-10 watershed comprises the Susquehanna Shale Hills Critical Zone Observatory (SSHCZO; Brantley et al., 2018b). Lastly, data were downloaded for two sites in the Juniata River Basin (HUC8; Figure 1c) and nine sites in the Susquehanna River Basin (SRB; HUC4; Figure 1d) from the Water Quality Portal (WQP; Read et al., 2017), a national repository for water quality data. These sites were selected based on the following criteria: (a) they were located along the main stem of the river, and (b) they provided >15 samples where aqueous Ca^{2+} , Mg^{2+} , Na^+ , K^+ , Cl^- , NO_3^- , and SO_4^{2-} , were all measured between 2014 and 2020. All data from the WQP were accessed and downloaded using dataRetrieval, an R package developed by the United States Geological Survey (USGS; De Cicco et al., 2018).

To disentangle effects related to watershed scale from those related to presence/absence of coal, we also retrieved data from watersheds in the Western United States. For these watersheds, we do not apply the machine learning model (see Section 2.3) to separate the sources of sulfate due to computational limitations. Instead, we target watersheds where pyrite is expected to be the predominant source of sulfate by querying for watersheds that meet five criteria. Specifically, these watersheds: (a) are located west of longitude -104° to minimize the effects of acid rain (longitude determined using acid deposition maps from the National Atmospheric Deposition Program; <http://nadp2.slh.wisc.edu/data/animaps.aspx>); (b) are characterized by <5% agricultural land use to minimize the effects of fertilizers; (c) are reported to not show major evaporite (i.e., gypsum) deposits at land surface to minimize the effect of other mineral sources of sulfate; (d) are characterized by a positive water balance (precipitation/potential evapotranspiration >1) to minimize the effects of evaporation; (e) provide >15 concentration-discharge ($C-q$) measurements for analysis. We identified 291 watersheds that met these criteria. These criteria do not ensure that pyrite is the only source of sulfate but are likely to minimize the impacts of the other contributing sources to the total sulfate budget.

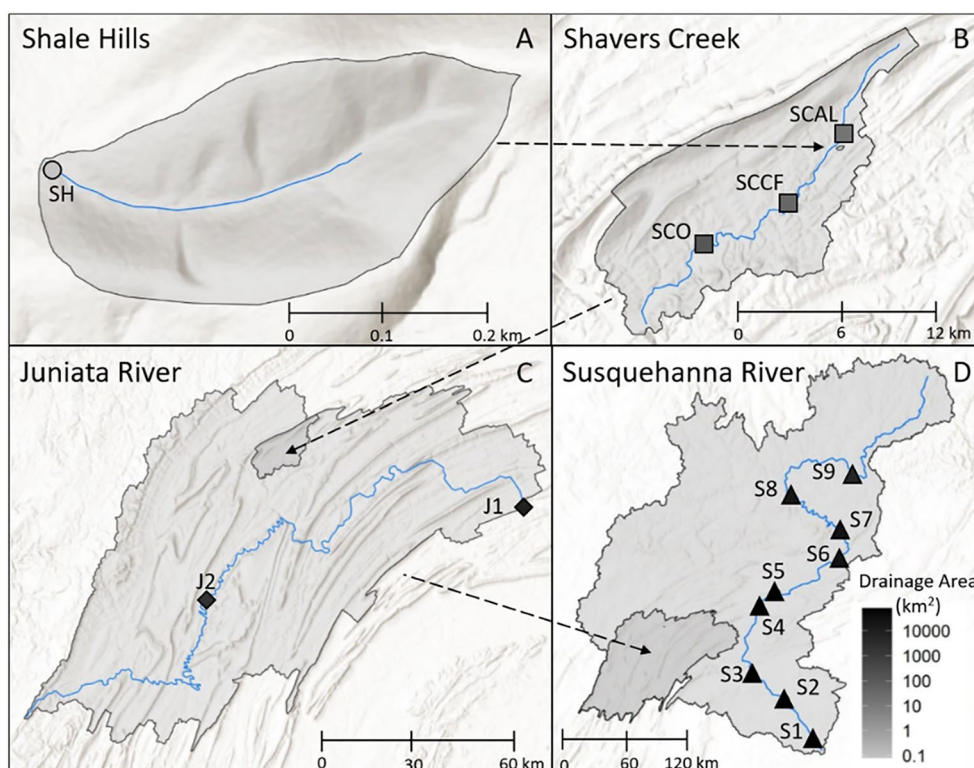


Figure 1. Maps showing the sampling locations for surface water sites and relationships of the four nested watersheds: (a) Shale Hills, (b) Shaver's Creek (SCAL, SCCF, and SCO), (c) Juniata River (J1 and J2), and (d) Susquehanna River (S1–S9). Shapes refer to river basin and intensity of shading indicates relative drainage area of the sub-catchments (light, smaller, dark, larger). Samples within Shale Hills and Shaver's Creek were collected by the SSHCZO and samples within the Juniata River and Susquehanna River were collected by the USGS and USEPA (Table S3 in Supporting Information S1).

2.2. Water Sampling and Analysis

Although much of the Shaver's Creek data has been published as referenced above, some waters were also sampled in this study using identical sampling approaches. For routine sampling, we collected stream water and split the sample into two subsamples. For cation analysis, we filtered the sample through a 0.45 μm filter and field-acidified to $\text{pH} < 2$ using 10% nitric acid. For anion analysis, we filtered the sample through a 0.45 μm filter and left the sample unacidified. All samples were stored at temperatures 5°C before analysis. Cation concentrations were measured on a Thermo Scientific iCAP 7400 Inductively Coupled Atomic Emissions Spectrometer and anion concentrations were measured on a Dionex Ion Chromatograph.

Additionally, an optical sensor (Campbell Scientific CS511) was deployed 20 m below land surface (mbls) in a well (CZMW11) at Shale Hills to measure DO concentrations over time from 2019 to 2020. A stage sensor (MeterGroup Hydros 21) was also deployed to monitor water level depth during the same time interval. Measurements were taken every 15 min and stage measurements were corrected to account for instrumental drift (Shaughnessy et al., 2021). All data for these sensors can be found on the SSHCZO website (http://www.czo.psu.edu/data_time_series.html).

On two sampling campaigns, surface water and groundwater were collected over the course of 2 days throughout the SSHCZO (Shale Hills [Figure 1a, Cole Farm, Garner Run, Shaver's Creek (Figure 1b); see Brantley et al., 2018b for site details]) for sulfur isotope compositions of sulfate (i.e., $\delta^{34}\text{S}$, reported in units of permil, ‰; Table S2 in Supporting Information S1). These samples were vacuum filtered through a 0.2 μm filter in the laboratory. Then, samples were dripped through an ion exchange column packed with 5 g of Cl^- type Bio Rad 1-X8 anion exchange resin. Before introducing each sample, ion exchange columns were pre-cleaned by triple rinsing with 3 M hydrochloric acid and then triple rinsing with deionized water. Once loaded, sulfate from each sample was eluted with 45 mL of 0.8 M hydrochloric acid as described in Le Gendre et al. (2017). This approach isolates

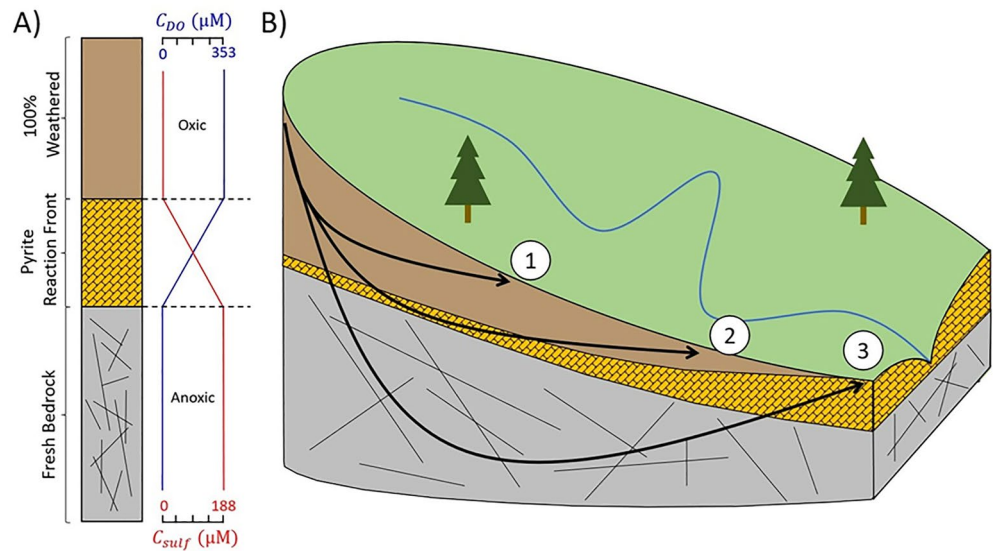


Figure 2. (a) Schematic representation of (left) a weathering profile under a ridgetop (where we assume one-dimensional, vertical water flow) and (right) schematic depth profiles for pyrite-derived sulfate and dissolved oxygen concentrations (i.e., C_{sulf} and C_{DO} , respectively) in the downward-flowing groundwater based on consumption of dissolved oxygen (DO) via pyrite oxidation across the pyrite reaction front under ridgetops. (b) 3-D cross-sectional view of a schematic watershed showing the subsurface pyrite oxidation zone (yellow) and hypothetical subsurface flow paths: (1) above the oxidation front, (2) partially through the front, and (3) through the reaction front. In both (a and b), the pyrite reaction front (yellow) is defined as the zone where oxidation is actively occurring and pyrite is still present but is partially depleted. Above the oxidation zone (i.e., brown), pyrite has been 100% oxidized, leaving secondary iron oxide minerals. Below the oxidation zone, negligible oxidation is occurring; therefore, this zone is fresh, pyrite-containing bedrock. Except for a few upward-connected fracture sets (Gu, Rempe, et al., 2020), oxidation does not occur below the oxidation front because DO is completely depleted as water travels through the oxidation front (a). This means that groundwater above the reaction front is generally oxalic and below the reaction front is anoxic.

sulfate and removes potential contamination by other anions (e.g., nitrate). Once eluted, sulfate was precipitated as barite (BaSO_4) by adding 5 mL of saturated BaCl_2 in deionized water. Barite was then centrifuged and rinsed 3x with deionized water and dried for isotope analysis.

For isotope analysis, $\sim 0.3\text{--}0.4$ mg of barite was weighed into a tin boat along with an excess ($\sim 5\times$) of vanadium pentoxide (V_2O_5) to ensure consistent ^{18}O abundance in resulting SO_2 analyte gas, as $^{32}\text{S}^{18}\text{O}^{16}\text{O}$ will isobarically interfere with $^{34}\text{S}^{16}\text{O}^{16}\text{O}$ (e.g., Fry et al., 2002). Samples were dried at least overnight in a vacuum oven prior to analysis on a Thermo Flash EA coupled to a Thermo Delta V isotope ratio mass spectrometer operated in continuous flow mode. Results are reported on the Vienna Canyon Diablo Troilite scale by analyzing a 3-point suite of international reference standards between every 10 samples (IAEA SO-5, $\delta^{34}\text{S} = +0.5\text{‰}$; IAEA SO-6, $\delta^{34}\text{S} = -34.1\text{‰}$; NIST NBS127, $\delta^{34}\text{S} = +20.3\text{‰}$). Samples were analyzed in duplicate and uncertainty is reported as the difference between duplicate measurements; long-term precision of standard reference materials was always better than $\pm 0.3\text{‰}$ (± 1 std. dev.).

2.3. Rock Sampling and Analysis

In addition to water samples, in-place bedrock was sampled from outcrops within the streambed at various locations within Shaver's Creek catchment (Figure S1 in Supporting Information S1; Table S4 in Supporting Information S1) in order to investigate the subsurface distribution of minerals (e.g., Figure 2). These samples were either collected from the surface using a rock hammer or recovered using a Shaw Portable Core Drill. The pulverized samples ($<150\ \mu\text{m}$) were analyzed for the concentration of total sulfur (Gu, Rempe, et al., 2020) and the values were compared to unweathered bedrock to estimate the extent of pyrite oxidation by assuming pyrite is the main sulfur-bearing mineral. A few thin sections were made by cutting across the center of the rocks and were checked under scanning electron microscopy (SEM). The elemental compositions of spots within the thin section were determined by energy dispersive X-ray spectroscopy (EDS). Based on the bulk analysis of total sulfur and

microscopic observations from SEM and EDS, the samples were classified as either fully oxidized, partially oxidized, or unoxidized with respect to pyrite (Figure S1 in Supporting Information S1).

2.4. Machine Learning Model

To separate the sources of sulfate, we utilize a machine learning-based mixing model called Non-negative Matrix Factorization (NMF) (Shaughnessy et al., 2021). In short, NMF determines the chemistry of the endmembers and the mixing proportions simultaneously. As a “blind source separation”, the user does not stipulate an endmember chemistry a priori; rather, NMF identifies endmember water chemistries and then geochemists must interpret the identity of the endmember based on understanding of the system. We chose to use the NMF-based mixing model rather than a more traditional technique because the large geographic extent of the SRB and the geological complexity of the region make it difficult to constrain the endmember chemistries. There are methods to solve for under-constrained endmember chemistries using more traditional inverse methods (e.g., Cole et al., 2022; Kemeny & Torres, 2021); however, due to our previous success at utilizing NMF at Shale Hills (Shaughnessy et al., 2021) and in other regions (e.g., Epuna et al., 2022; Shaheen et al., 2022), we chose to utilize NMF here as well. NMF also provides the benefit that it does not rely a priori on assumptions about water chemistry of endmembers.

NMF decomposes a matrix of stream chemistry, V (dimensions = $n \times m$), into the product of two matrices, W and H . The m columns of V are concentration ratios $[X]/[\text{SO}_4^{2-}]$, where brackets denote molar concentration and $X = \text{Ca}^{2+}$, Mg^{2+} , Na^+ , K^+ , Cl^- , and NO_3^- . The n rows of V are samples taken at different sampling dates for a given site or group of sites. W has the dimensions $n \times p$, where n is the number of sampling dates and p is the number of endmembers. The cell entries of W are the mixing proportions of the endmembers. The row sum of each entry in W is constrained to equal 1.00 ± 0.05 , meaning that the stream chemistry is completely described (± 0.05) as a combination of endmembers. This is referred to as a unity constraint. H has the dimensions $p \times m$ and its cell entries represent the chemical signature of each of the endmembers.

As used here, NMF is governed by a series of mass balance equations and the only parameter that needs to be set before the model is run is p —the number of endmembers. We utilize principal component analysis (PCA) to determine the number of components that are needed to explain >90% of the variation in the stream ratio data and we define this value as p . This number of components represents the smallest number of endmembers needed to “unmix” the stream chemistry. For our analysis, we utilize the “prcomp” function from the “stats” package in R. PCA has been used elsewhere to determine the number of endmembers in a mixture as well (e.g., Christophersen & Hooper, 1992). We developed this approach of using PCA by running the model using many different numbers of endmembers (2, 3, 4, etc.) and then comparing the results to our geochemical knowledge of the system. We discovered that for all of the watersheds we have investigated with our technique, the PCA analysis yielded results that are consistent with our geochemical knowledge, as well as revealing the “correct” endmember chemistries for synthetic data sets (see Shaughnessy et al., 2021). This is the motivation behind using PCA to determine the number of endmembers.

The solution for NMF is non-unique; therefore, we run the model 10,000 times to account for variability in the derived endmember compositions and mixing proportions. We filter out any models that do not fulfill the unity constraint. Additionally, following Shaughnessy et al. (2021), we filter out poor-fitting models and retain only the fifth percentile of best-fitting models. These are averaged and reported here. For both the PCA and NMF calculations, we utilize default parameters in R and SK-learn algorithm implementations, respectively.

The validity of the NMF modeling was investigated by Shaughnessy et al. (2021). In our previous study, we created a synthetic data set where the mixing proportions and the endmember chemistries (H) were known, but not input into the model. We found that NMF successfully derived the correct endmember chemistries and mixing proportions for the synthetic data set. In addition, we compared sulfur isotopes and calcite saturation indices to the modeling results for samples from Shale Hills. We found that when pyrite-derived sulfate concentrations were high (as determined by NMF), sulfur isotopes showed a depleted signature that is consistent with pyrite at Shale Hills (see Figure 4a in Shaughnessy et al., 2021), and the water was saturated with respect to calcite, which is consistent with sulfuric acid driving dissolution of the ubiquitous mineral, calcite, at depth. Both of these observations are consistent with pyrite oxidation, which supports that our model identifies the pyrite-sulfate signal in the stream chemistry and separates pyrite-sulfate from other sulfate sources such as acid rain or fertilizer.

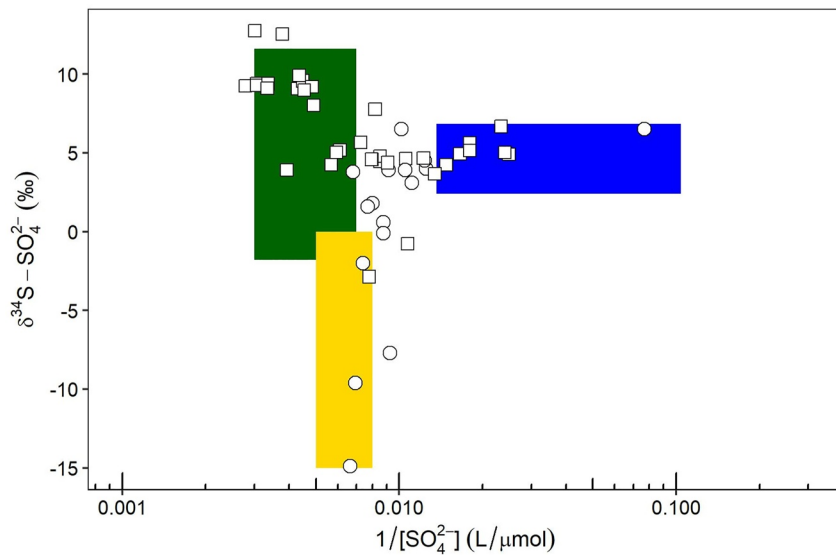


Figure 3. Plot showing sulfur isotope values in stream sulfate (i.e., $\delta^{34}\text{S}$) plotted versus the reciprocal of sulfate concentration $[\text{SO}_4^{2-}]$ (μM) for surface and groundwater samples across the Shaver's Creek watershed. Sulfur isotope ranges shown for fertilizer (i.e., the y-axis range for green rectangle) are from a global compilation (Zhang et al., 2015), and the concentration range (i.e., the x-axis range) is inferred from measurements of sulfate in groundwater near a farm field in Shaver's Creek (i.e., Cole Farm Well CFW4; see Forngeng, 2021 for well location). Sulfur isotope and concentration ranges for pyrite oxidation are also shown (yellow rectangle) as inferred for pyrite oxidation at Shale Hills (Jin et al., 2014). The range of values for acid rain (blue rectangle) are based on measurements of rain chemistry at Hubbard Brook, a watershed ~ 600 km to the northeast (Alewell et al., 2019). Circles are surface and groundwater samples from Shale Hills reported by Jin et al. (2014) and squares are surface and groundwater samples collected throughout the SSHCOZ in this study.

2.5. Data Analysis

First, for the Shaver's Creek analysis, stream samples were utilized in the NMF model (Section 2.3) to separate the sources of sulfate. From the NMF decomposition for Shaver's Creek and the H matrix, the endmember chemistries were then attributed to sources using sulfur isotopes and site-specific and geochemical knowledge. After developing the Shaver's Creek model, we constructed models for the Juniata and Susquehanna River sites similarly (Figures 1c and 1d).

After NMF, we utilized the pyrite-derived sulfate concentrations, C_{sulf} , in an oxidation model for each site (see Section 4.1; Equation 10). Following a published approach (i.e., Ibarra et al., 2016), we fit the oxidation model to the concentration and discharge data using a nonlinear least squares model. We utilized the 95th percentile value of concentration for each stream as the starting point for each of the nonlinear least squares models (Ibarra et al., 2016) and the Gauss-Newton algorithm to solve for model parameters (i.e., Dw and $C_{\text{sulf}}^{\text{max,obs}}$; Equation 10). All model calculations were performed in R using the “nls2” package (Grothendieck, 2013).

3. Results

3.1. Sources of Sulfate

Following our previous approach for Shale Hills where two components (i.e., pyrite oxidation and acid rain) were observed to explain stream sulfate concentrations (Shaughnessy et al., 2021), we investigated pyrite oxidation in the larger and encompassing HUC-10 watershed of Shaver's Creek. For that data set, PCA revealed three components were needed to explain $>90\%$ of the variance in stream chemistry. Given that Shaver's Creek has agricultural land use, we anticipated that the three sources of sulfate would be the two identified at Shale Hills (acid rain, pyrite) and an additional sulfate source, fertilizer.

Sulfur isotopic measurements are also consistent with three inferred sources of sulfate in Shaver's Creek (Figure 3). In particular, the isotopic signature of dissolved sulfate in Shaver's Creek water falls between the inferred compositions of three sources inferred to be acid rain, pyrite, and fertilizer. For example, the $\delta^{34}\text{S}$ values in shallow

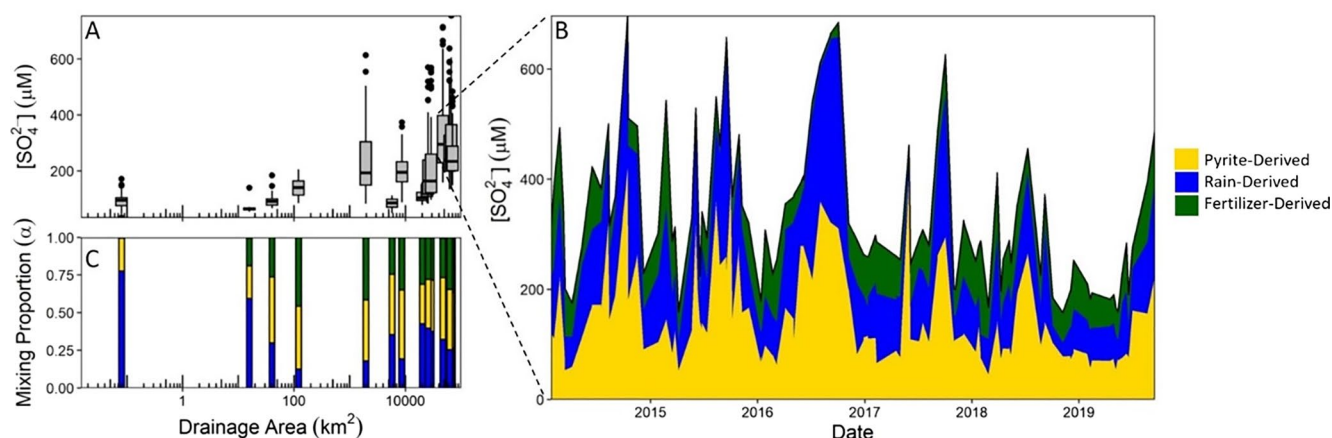


Figure 4. (a) Plot showing the average concentration of sulfate at sites in the Susquehanna River Basin (SRB). (b) Plot showing an example of the temporal series of sulfate concentrations broken down by source for site S4 in the SRB as determined by Non-negative Matrix Factorization (see Figure 1d). (c) Plot showing the average mixing proportions of sulfate sources for each site.

groundwater near a farm field are consistent with measurements of fertilizer sulfate as reported elsewhere (Zhang et al., 2015). In contrast, the $\delta^{34}\text{S}$ values in groundwater in a non-agricultural subcatchment within Shaver's Creek that is underlain by sandstone (i.e., Garner Run) are consistent with acid rain. A third sulfate source in Shaver's Creek is inferred from the $\delta^{34}\text{S}$ values in deep groundwater at Shale Hills: these are much depleted, ranging from -15‰ to 0‰ , consistent with pyrite oxidation (Jin et al., 2014). The isotopic signature of dissolved sulfate in Shaver's Creek water falls in between the inferred compositions of acid rain, pyrite, and fertilizer, as expected if these three endmembers contribute sulfate to Shaver's Creek (Figure 3).

Based on the PCA and the isotope data, we set the number of endmembers (i.e., p) in the NMF model to 3. After running the model, the derived geochemical signatures for each of the three endmembers are distinct (Table S1 in Supporting Information S1). We use geochemical knowledge to identify these sources. Comparing results from Shaver's Creek to the non-agricultural shale-underlain headwater catchment of Shale Hills, we identify the first two sulfate sources in Shaver's Creek as pyrite oxidation and acid rain (Shaughnessy et al., 2021). Pyrite oxidation can be identified because oxidation releases sulfuric acid which, in sedimentary rock, causes dissolution of (Ca, Mg) carbonate minerals at depth, releasing Ca^{2+} and Mg^{2+} to ground waters (Calmels et al., 2007; Torres et al., 2016). Furthermore, dissolution of carbonate minerals has been observed to accompany pyrite oxidation at Shale Hills in hand samples from depth (Gu, Mavko, et al., 2020). Therefore, the source with the highest ratios of $[\text{Ca}^{2+}]/[\text{SO}_4^{2-}]$ and $[\text{Mg}^{2+}]/[\text{SO}_4^{2-}]$ is identified as pyrite oxidation. To identify the acid rain endmember, we note that rain sometimes retains the Na/Cl ratio of ocean water, 0.86 (Möller, 1990; Neal & Kirchner, 2000), very close to that of endmember 2, 0.89 (Table S1 in Supporting Information S1). The third endmember in the Shaver's Creek model has the highest $[\text{NO}_3^-]/[\text{SO}_4^{2-}]$ ratio, which is consistent with sulfate-containing fertilizer application in the watershed. A breakdown of the average source contributions per site can be found in Figure 4c.

3.2. DO Dynamics

The reactant driving pyrite oxidation is DO at the reaction front (Gu, Rempe, et al., 2020). In Figure 5b, we show the concentration of DO, C_{DO} , measured from 2020 to 2021 in groundwater from a borehole (CZMW11) located toward the outlet of the watershed at Shale Hills. The DO probe was placed at 20 mbls within the reaction front, the depth of which was determined via solid phase analysis of drill cuttings (Gu, Rempe, et al., 2020). Although sampled in different years, the seasonal trends of pyrite-derived sulfate, C_{sulf} (sampled 2008–2010), in the stream and C_{DO} (sampled 2020–2021) in groundwater are opposite. C_{sulf} is high in the dry season and low in the wet season, while C_{DO} is high in the wet season and low in the dry season.

3.3. Streambed Pyrite in Shaver's Creek

The extent of pyrite oxidation observed in intact bedrock from the stream bed varied downstream in Shaver's Creek (Table S4 in Supporting Information S1). In the samples where thin sections were made, euhedral or

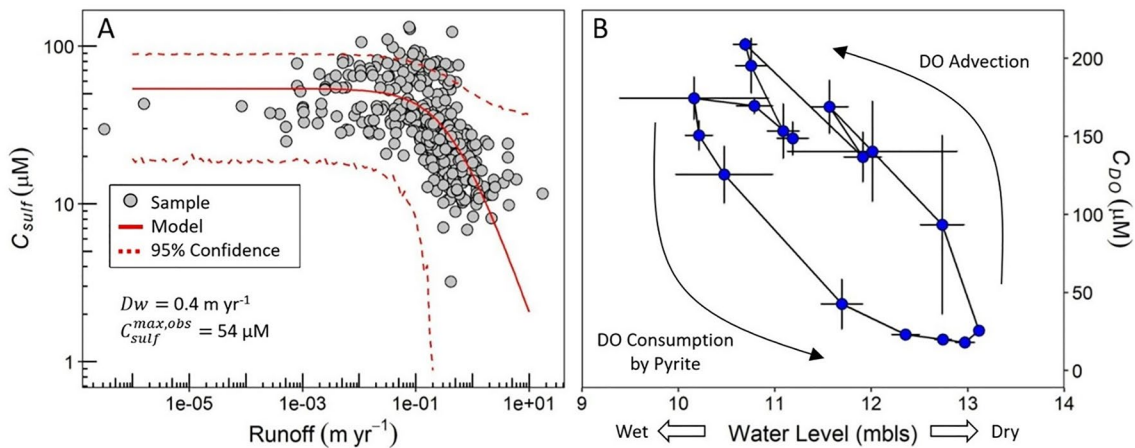


Figure 5. Concentration-discharge relationship for pyrite-derived sulfate concentrations measured in the outlet stream at Shale Hills (a) measured during 2008–2010. The solid line is the fit of Equation 2 to the data, and the dashed lines are the 95% confidence intervals. (b) shows the monthly average dissolved oxygen (DO) concentration in groundwaters collected at 20 mbls in a borehole near the outlet (CZMW11) at Shale Hills from 2020 to 2021 plotted versus the water table depth. Arrows in (b) indicate the general trend over time. First, DO is advected to the sensor in the wet season and then DO is depleted in the dry season.

framboidal pyrite was observed in unoxidized samples via SEM. Where oxidation had occurred, we observed iron oxide pseudomorphs after pyrite, similar to those observed at depth under Shale Hills previously (Gu, Heaney, et al., 2020; Gu, Rempe, et al., 2020). The pseudomorphs document pyrite that has been oxidized in the subsurface. The elemental compositions of the oxidized framboids were determined by EDS and the pseudomorphs were found to contain no sulfur. We found that in some samples, pyrite framboids and iron oxide pseudomorphs were both present, which we refer to as partially oxidized samples. In the upper part of Shaver's Creek watershed, pyrite in outcrops within the streambed was fully or partially oxidized, whereas pyrite in downstream outcrops was predominantly unoxidized (Figure S1 in Supporting Information S1). Location and lithologic formation data be found in Table S4 in Supporting Information S1.

3.4. Concentrations Across Watershed Scale

The average sulfate concentrations in the stream waters increase as the size of the drainage basin increases (Figure 4a). At the outlets of Shale Hills, Shaver's Creek, the Juniata River, and the Susquehanna Rivers, for example, the average sulfate concentrations are 95 ± 17 , 114 ± 23 , 160 ± 37 , and $223 \pm 57 \mu\text{M}$, respectively. All sites show similar seasonal trends in stream sulfate concentrations, where sulfate concentrations are highest in the summer and fall and lowest in the winter and spring.

The relative proportions of sulfate sources, namely pyrite and acid rain fractions, change both temporally (seasonally) and with increasing spatial scale. The proportions of acid rain sulfate are larger in small watersheds, and as the watershed size increases, the proportions of sulfate from pyrite and fertilizer both increase (Figure 4c). In all watersheds, we observe the highest proportion of pyrite-derived sulfate in the summer and fall and the highest proportion of acid rain in the winter and spring (Figure 4b), a trend previously observed for the subcatchment of Shale Hills (Shaughnessy et al., 2021). We observe no significant temporal trend in fertilizer-derived sulfate, likely due to the pervasive legacy fertilizers present in groundwater in the SRB (e.g., Van Meter et al., 2017).

4. Discussion

4.1. Oxidation Model

To explore river and groundwater sulfate dynamics, we propose a simple model that describes pyrite oxidation along a flow path as recorded in variations in stream chemistry. There are many oxidation reactions that remove O_2 from groundwater. Some of the electron donors in these reactions include soil organic carbon, petrogenic organic carbon, and redox-sensitive minerals such as pyrite (Gu, Rempe, et al., 2020) and chlorite (Liao et al., 2022). We assume that oxidation of the modern organic matter occurs strictly in the soil and sediment, affecting the initial DO concentrations entering the underlying rock (as described below). In contrast, petrogenic organic matter can

oxidize in the rock or in the soil. In general, however, pyrite is usually observed to be the first mineral to oxidize in bedrock. For example, observations document that pyrite tends to be depleted by oxidation before all the petrogenic organic carbon is oxidized (Bolton et al., 2006; Hemingway et al., 2018; Petsch et al., 2000). Furthermore, although the exact depth of the front in Shale Hills is difficult to measure, the concentration of petrogenic organic carbon is very low and the extent of depletion is smaller than pyrite (Ogrič et al., 2023). For this reason, we focus on pyrite oxidation because it is likely the deepest oxidation occurring in the bedrock.

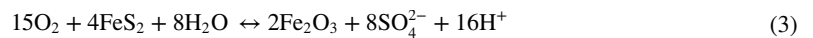
Following other simple weathering model treatments (e.g., Berner, 1978; Kump et al., 2000), the change of pyrite-derived sulfate concentrations, C_{sulf} (mol m⁻³), in stream waters over time, t , is a balance between dilution and R , the rate of pyrite oxidation (mol sulfate m⁻³ yr⁻¹):

$$\frac{\partial C_{\text{sulf}}}{\partial t} = R - C_{\text{sulf}} \frac{Q}{V} \quad (1)$$

For simplicity, we abbreviate pyrite-generated sulfate as p-sulfate. In Equation 1, Q is the volumetric flow rate of water through the system (m³ yr⁻¹) and V is the volume of water stored in the watershed (m³). The rate of oxidation, R , at the mineral surface can furthermore be expressed for any packet of water moving through the watershed as follows:

$$R = -\frac{\partial C_{\text{DO}}}{\partial t} = k_1 C_{\text{DO}} \quad (2)$$

Here, k_1 is the rate constant (yr⁻¹) and C_{DO} is the concentration of DO in the groundwater, specifically within the fractures of the oxidation zone where groundwater flows. Here, we assume that the packet of fluid can continue interacting with pyrite in the bedrock until all the DO is consumed. Next, we rewrite R with respect to C_{sulf} , rather than C_{DO} . To transform from C_{DO} to C_{sulf} , we note that 15 mol of O₂ are consumed for every 8 mol of sulfate produced (where the equation is written under the assumption that all iron precipitates as hematite):



The concentration of DO in water entering the subsurface is assumed to be equilibrated either with O₂ in the atmosphere or, if other mineral or organic matter reductants are present in the soil, with the soil atmosphere at the soil-bedrock interface. Here, we denote either concentration as $C_{\text{DO}}^{\text{atm}}$. If water (at 10°C) is in equilibrium with the atmosphere, $C_{\text{DO}}^{\text{atm}}$ equals 353 μM and if in equilibrium with the soil atmosphere at the base of soil in Shale Hills, this value equals about 260 μM (Gu, Heaney, et al., 2020; Gu, Rempe, et al., 2020). For any packet of water that enters the subsurface with $C_{\text{DO}}^{\text{atm}}$ and then reacts with pyrite, the stoichiometry of reaction 3 dictates that:

$$C_{\text{DO}} = C_{\text{DO}}^{\text{atm}} - \frac{15}{8} C_{\text{sulf}} \quad (4)$$

We define the concentration of sulfate after reaction with pyrite where $C_{\text{DO}} = 0$ as $C_{\text{sulf}}^{\text{max,pred}}$. Given this definition and the stoichiometry of reaction 3,

$$C_{\text{sulf}}^{\text{max,pred}} = \frac{8}{15} C_{\text{DO}}^{\text{atm}} \quad (5)$$

Substituting Equations 4 and 5 into Equation 2 yields

$$R = k_1 \frac{15}{8} (C_{\text{sulf}}^{\text{max,pred}} - C_{\text{sulf}}) \quad (6)$$

Inserting Equation 6 into Equation 1, and solving for steady-state concentration of sulfate (i.e., $\frac{\partial C_{\text{sulf}}}{\partial t} = 0$) results in:

$$C_{\text{sulf}} = \frac{k'_1 C_{\text{sulf}}^{\text{max,pred}}}{k'_1 + k_f} = \frac{k'_1 C_{\text{sulf}}^{\text{max,pred}} z}{k'_1 z + q} \quad (7)$$

Here, we have rewritten the rate constant to include the stoichiometric coefficient ($k'_1 = \frac{15}{8} k_1$). In the derivation of Equation 7, we assumed that V is constant while Q varies. Again, following a previous treatment (Berner, 1978), the frequency that the watershed is flushed, Q/V , is defined as k_f (yr⁻¹) and the inverse of k_f is the residence time

for water in the watershed. The assumption that V in a watershed is constant must be incorrect to some extent depending upon the time frame of analysis (e.g., Birkel et al., 2011; Kirchner, 2009). This assumption will impact the transit time distribution of flow paths entering the stream, which has been shown to change the shape of the concentration-discharge curve (Torres & Baronas, 2021). We note that this is a limitation to our approach, but this parsimonious model is a starting point that allows us to compare concentration-discharge dynamics across watersheds where the transit time distributions are unknown. This assumption is also roughly equivalent to the hypothesis of exponential transit times and is thus consistent with the treatment by Maher and Chamberlain (2014).

Conceptualizing the watershed as a one-dimensional chemical reactor in these equations, we furthermore consider the flushing frequency in terms of runoff q (m yr^{-1}) along an average representative flow path of length z : $q = zk_f$. Both of the terms are in the denominator of Equation 7 can then be related to the Damköhler number, Da , for a watershed:

$$Da = \frac{k'_1}{k_f} = \frac{k'_1 z}{q} \quad (8)$$

In effect, Da is the ratio of the characteristic time scale of advection divided by that of dissolution. When $Da \gg 1$, reaction is fast compared to transport ($k'_1 \gg k_f$) and the system is transport-limited, but when $Da \ll 1$ ($k'_1 \ll k_f$), the system is kinetic- or reaction-limited. For chemical engineers, Da is usually expressed as a function of the length of the chemical reactor z . For the simple approximation for a watershed presented here, z can be considered to be the length of the weathering flow path (Brantley & Lebedeva, 2021). Conceptually, for kinetic-limited oxidation (where $Da \ll 1$), water leaves the watershed before it reaches equilibrium for the mineral reaction but for transport limitation where $Da \gg 1$, water leaves the watershed after equilibration. We can then substitute Equation 8 into Equation 7, which results in:

$$C_{\text{sulf}} = \frac{C_{\text{sulf}}^{\text{max,pred}} Da}{Da + 1} = \frac{C_{\text{sulf}}^{\text{max,pred}} Dw}{Dw + q} \quad (9a)$$

$$Da = \frac{Dw}{q} \quad (9b)$$

$$Dw = k'_1 z \quad (9c)$$

Maher and Chamberlain (2014) define a new term Dw as the Damköhler coefficient (m yr^{-1}), which we adopt here shown in Equation 9b. These authors use C^{eq} (i.e., concentration of solute in equilibrium with the bedrock) instead of C^{max} in their model. In later iterations of the model (Ibarra et al., 2016), they replace C^{eq} with C^{max} , which is the empirical maximum solute concentration. Their results for weathering reactions in many watersheds (Ibarra et al., 2016) show that C^{max} is often less than what would be expected at equilibrium. Based on this observation, we also replace $C_{\text{sulf}}^{\text{max,pred}}$ (a theoretical equilibrium value) with $C_{\text{sulf}}^{\text{max,obs}}$ (an empirical, observed value) in Equation 9a and derive the following expression:

$$C_{\text{sulf}} = \frac{C_{\text{sulf}}^{\text{max,obs}} Dw}{Dw + q} \quad (10)$$

Although derived differently, Equation 10 is mathematically equivalent to the solute production model (SPM) previously proposed (Maher & Chamberlain, 2014), when C_0 (the initial concentration of solute entering the watershed) in the original SPM equals zero. Because we first use an inverse model to separate the sources of solutes (i.e., NMF), C_0 in our model implicitly equals zero (pyrite oxidation only occurs in the watershed). The SPM has been used by several authors to fit C - q data for silicate weathering (Ibarra et al., 2016; Wymore et al., 2017), carbonate weathering (Zhong et al., 2020), and global weathering patterns (Ibarra et al., 2017; Maher & Chamberlain, 2014); however, this study is the first time that the model is linked to the subsurface distribution of minerals. We determined $C_{\text{sulf}}^{\text{max,obs}}$ and Dw for each watershed here by fitting measurements of C_{sulf} versus q to Equation 10 using nonlinear least squares regression.

The flux of p-sulfate, F_{pyrite} , is manifested in stream chemistry as the product of C_{sulf} and q and thus, using Equation 10, we can write

$$F_{\text{pyrite}} = qC_{\text{sulf}} = \frac{qC_{\text{sulf}}^{\text{max,obs}} Dw}{Dw + q} \quad (11)$$

When q is very small, $F_{\text{pyrite}} \approx qC_{\text{sulf}}^{\text{max,obs}}$ and $C_{\text{sulf}} \approx C_{\text{sulf}}^{\text{max,obs}}$ (Equations 10 and 11), which means that p-sulfate concentrations are constant, and the rate of pyrite oxidation linearly increases with runoff. This behavior is interpreted as pyrite oxidation limited by transport of DO into or sulfate out of the system (advective transport-limited oxidation). When q is very large, $F_{\text{pyrite}} \approx C_{\text{sulf}}^{\text{max,obs}} Dw$ and $C_{\text{sulf}} \approx \frac{C_{\text{sulf}}^{\text{max,obs}} Dw}{q}$ (Equations 10 and 11), which means that p-sulfate concentrations are inversely proportional to runoff and the pyrite oxidation rate is constant. In this regime, the rate of oxidation cannot keep up with the rate of dilution (kinetic- or reaction-limited oxidation).

Next, we interpreted our oxidation model with respect to the subsurface redox architecture across small and large watersheds. First, we remind the reader that $C_{\text{sulf}}^{\text{max,pred}}$ is the maximum concentration of p-sulfate in groundwater predicted after complete consumption of DO. As discussed earlier, we assume water at 10°C (i.e., the average temperature of groundwater at Shale Hills) is equilibrated with atmospheric oxygen (i.e., DO = 11.3 mg/l or 353 μM) and reacts with pyrite until DO reaches zero. Given these assumptions, $C_{\text{sulf}}^{\text{max,pred}}$ equals 188 μM. Although $C_{\text{sulf}}^{\text{max,pred}}$ varies slightly with temperature, we assume that $C_{\text{sulf}}^{\text{max,pred}} = 188 \mu\text{M}$ everywhere for simplicity.

We suggest five reasons why $C_{\text{sulf}}^{\text{max,obs}}$ could be less than $C_{\text{sulf}}^{\text{max,pred}}$. First, our NMF decomposition could simply be attributing too much sulfate to other sources, inaccurately lowering the concentration of p-sulfate. Second, water entering the subsurface could be in equilibrium with soil gases rather than atmospheric gases. At Shale Hills, soil gas O₂ concentrations are 75% of PAL at the base of the soil; therefore, groundwater in equilibrium with soils should have DO concentrations of 260 μM (8.3 mg/l; Gu, Rempe, et al., 2020; Hodges et al., 2019). Third, other redox-sensitive species in the bedrock (e.g., petrogenic organic matter, chlorite, and ankerite) could consume DO before the oxygen reaches pyrite. The relative importance of each electron donor in removing DO is determined by the distribution, concentration, and oxidation kinetics of each species in the bedrock. Fourth, there could be too little pyrite in the bedrock to completely deplete the DO for a given packet of water and flow path. In this situation, then the groundwater that emerged into the stream will still contain DO. Lastly, the depth of groundwater flow might be less than the depth of the pyrite reaction front. A typical weathering profile from Shale Hills and other shale-underlain watersheds (Gu, Rempe, et al., 2020) for pyrite is shown in Figure 2a. Based on this weathering profile structure, three generalized types of flow path are possible (Figure 2b): (a) above the reaction front such that water does not interact with pyrite and $C_{\text{sulf}} = 0$; (b) through part of the reaction front such that pyrite oxidation affects the water but does not deplete all DO, resulting in $C_{\text{sulf}} < C_{\text{sulf}}^{\text{max,pred}}$, and (c) completely through a reaction front that has enough pyrite to deplete the DO, such that $C_{\text{sulf}} = C_{\text{sulf}}^{\text{max,pred}}$ (Figure 2b). Flow paths 1 and 2 result in $C_{\text{sulf}}^{\text{max,obs}} < C_{\text{sulf}}^{\text{max,pred}}$.

Given the five explanations for understanding $C_{\text{sulf}}^{\text{max,obs}}$, only the last explanation (i.e., differing flow paths) has any implicit scaling relationship. In other words, the length and depth of flow paths can change as a function of drainage area, but it is unlikely that under-apportioning of p-sulfate (explanation 1), the relative importance of different redox reactions (explanations 2 and 3), or the concentration of pyrite in the bedrock (explanation 4) systematically varies with watershed size. For this reason, we infer that $C_{\text{sulf}}^{\text{max,obs}}$ can give clues to the average flow path and its position with respect to the reaction front.

Another way to understand the chemistry of each packet of water along a flow path is to consider the average length of flow of the packet through the reaction front, l , normalized by the length of the total flow path from the land surface to the stream (L). Those two quantities can be used to approximate the advective Damköhler number, Da , for a reaction under some circumstances (Brantley & Lebedeva, 2021):

$$Da = \frac{L}{l} \quad (12)$$

In defining this Damköhler number, the watershed is likened to a packed-bed chemical reactor where L is the length of the reactor and l is the length of the reaction zone. For $Da > 1$ ($L > l$), the system is transport-limited, and for $Da = 1$ ($L = l$), the system is kinetically limited (the derivation for this treatment does not allow $Da < 1$ because L cannot be smaller than l). We can determine the relative flow path length through the reaction front by converting Dw from our oxidation model to Da (i.e., $Da = Dw/q$) by multiplying by the mean runoff for each watershed.

4.2. Oxidation Model for Shale Hills

As discussed in Shaughnessy et al. (2021), there are two sources of sulfate at Shale Hills: pyrite oxidation and acid rain, and the NMF model successfully separates contributions in each stream sample from each source.

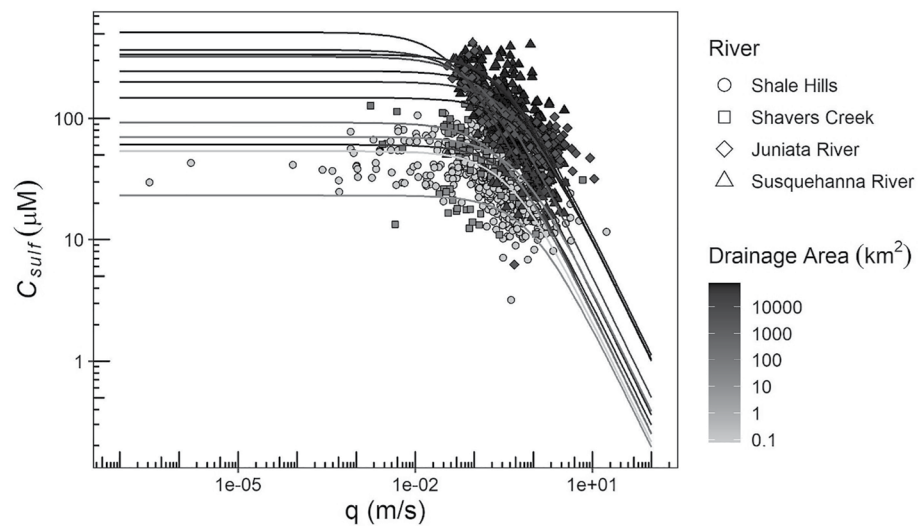


Figure 6. Plot showing the C - q relationships for all 14 sampling locations where symbols (NMF derived p-sulfate concentrations) are plotted on top of one another and lines refer to model fits to each sub-watershed. Gray scale as shown at right is used for lines and symbols to indicate drainage.

Using the oxidation model (Equation 10) and our NMF decomposition, we aimed to describe how the concentration of pyrite-derived sulfate (C_{sulf}) in the stream at Shale Hills changes as a function of runoff, q . At low q , C_{sulf} varies by a factor of ~ 5 , while at high q , C_{sulf} varies by a factor of ~ 30 . The relatively constant C_{sulf} at low q is consistent with pyrite oxidation limited by the transport of DO to the reaction front (i.e., advective transport limited). At high q , C_{sulf} is diluted to lower values, consistent with pyrite oxidation limited by reaction (reaction- or kinetic-limited). For Shale Hills, we observe both regimes as evidenced in the C - q curve shown in Figure 5a. Fitting Equation 10 to C_{sulf} and q , we find $C_{\text{sulf}}^{\text{max,obs}} = 54 \pm 2 \mu\text{M}$ and $Dw = 0.4 \pm 0.05 \text{ m yr}^{-1}$ ($p < 0.01$; Figure 5a).

At Shale Hills, $C_{\text{sulf}}^{\text{max,obs}} < C_{\text{sulf}}^{\text{max,pred}}$, regardless of whether we use soil O_2 or atmospheric O_2 to define $C_{\text{sulf}}^{\text{max,pred}}$. Using the conceptual model in Figure 2, we interpret this to mean that the stream mostly integrates flow paths above and partially through the reaction front with little contribution of completely oxygen-depleted water that travels in flow paths completely through the reaction front. However, we know that some groundwater flow paths at Shale Hills cross the pyrite reaction front. For example, Sullivan et al. (2016) collected groundwater samples from a ridgetop borehole (i.e., CZMW8) below the pyrite oxidation front as determined based on mineralogical analysis of borehole cuttings at depth. They found that the average sulfate concentration in the groundwater from this well at 30.1 mbls was $182 \pm 38.7 \mu\text{M}$ ($n = 9$), which is consistent with $C_{\text{sulf}}^{\text{max,pred}} = 188 \mu\text{M}$. Water that crosses the oxidation front entirely might not contribute significantly to the stream; therefore, it is not detected by our treatment, which emphasizes water in flow paths above and partially through the oxidation front.

The seasonality of C_{sulf} and C_{DO} is consistent with consumption of DO via pyrite oxidation at Shale Hills. We observe that C_{DO} increases seasonally (in CZMW11) as the water level in the borehole increases, that is, as the water table rises (Figure 5b). This is consistent with advection of groundwater with high DO to the reaction front—perhaps through interconnected fractures (Gu, Heaney, et al., 2020; Sullivan et al., 2016)—during the wet season. As the water level lowers, C_{DO} decreases sharply, likely due to pyrite oxidation removing DO from the groundwater (Figure 5b). Because the measurements shown in Figure 5 were made in water samples from 20 mbls (within the pyrite reaction front at the location of the borehole), it is unlikely that the removal of oxygen from the groundwater in this location is due to oxidation of other materials (e.g., organic matter).

4.3. C - q Analysis

Similar to Shale Hills (see Section 4.2), we calculated Dw and $C_{\text{sulf}}^{\text{max,obs}}$ for sites across Shaver's Creek, the Juniata River, and the Susquehanna River using the oxidation model. The oxidation model successfully described the C - q behavior for all the sampling points (watersheds) in the study, except for S9, the most upstream site in the SRB. For S9, we observe an increase in C_{sulf} as q increases, which cannot be described by our model. The fit of the model to the C - q data (for all sampling locations except for S9) can be seen in Figure 6. Generally, $C_{\text{sulf}}^{\text{max,obs}}$ increases and

D_w decreases with increasing drainage area. Small watersheds tend to show $C_{\text{sulf}}^{\text{max,obs}} < C_{\text{sulf}}^{\text{max,pred}}$ and large watersheds tend to show $C_{\text{sulf}}^{\text{max,obs}} > C_{\text{sulf}}^{\text{max,pred}}$. As discussed previously, values of $C_{\text{sulf}}^{\text{max,obs}} < C_{\text{sulf}}^{\text{max,pred}}$ are easy to explain; however, the conceptual model (Figure 2b) fails to explain $C_{\text{sulf}}^{\text{max,obs}} > C_{\text{sulf}}^{\text{max,pred}}$ in large watersheds. We explore this trend further in Section 4.4.

4.4. Explanations for $C_{\text{sulf}}^{\text{max,obs}} > C_{\text{sulf}}^{\text{max,pred}}$

4.4.1. Two Hypotheses

To explain why most large watersheds show $C_{\text{sulf}}^{\text{max,obs}} > C_{\text{sulf}}^{\text{max,pred}}$ in the SRB, we hypothesized that a different oxidant is present for the pyrite in larger watersheds. Fe^{3+} is a known oxidant for pyrite (Silverman, 1967), but ultimately, in a closed system, O_2 is needed to transform Fe^{2+} (produced during pyrite oxidation by Fe^{3+}) back to Fe^{3+} (i.e., regeneration of oxidant) and ferric iron concentrations are low at circumneutral pH; therefore, ferric iron is unlikely to be the missing oxidant unless the system is open to O_2 . Some studies have suggested that NO_3^- can oxidize pyrite (Juncher Jørgensen et al., 2009; Torrentó et al., 2011); however, this reaction must be microbially mediated. Pore throats in the pyrite-containing zone of the shale at Shale Hills are too small for microorganisms to access the pyrite; therefore, pyrite oxidation in these locations is abiotic (Gu, Rempe, et al., 2020). Although other watersheds might have larger pores, it is unlikely that pore size depends on watershed size; therefore, NO_3^- -dependent pyrite oxidation is also unlikely to explain the overall trends. We, therefore, concluded that an alternate oxidant alone is unlikely to explain our findings.

This led us to hypothesize that transport of O_2 to the mineral surface differed in large and small watersheds: in other words, oxidation in large watersheds is better described as open-system rather than close-system oxidation. If this is the explanation, then both Fe^{3+} and micro-organisms could be important in localities in the larger watersheds. Furthermore, the open-system nature is likely related to the importance of coal mining in impacting riverine sulfate dynamics in the SRB over the last many decades (Raymond & Oh, 2009). For example, coal mining in parts of the SRB has exhumed pyrite and exposed it at the surface, which allows direct interaction of pyrite with gaseous O_2 (i.e., an open system). The easy influx of O_2 in the air to mined layers could explain riverine concentrations of C_{sulf} and $C_{\text{sulf}}^{\text{max,obs}}$ greater than $C_{\text{sulf}}^{\text{max,pred}}$. We infer that as drainage area in the SRB increases, the probability that the watershed is impacted by coal mining increases (Figure S2b in Supporting Information S1). After mining coal in the larger watersheds, oxidation of pyrite becomes kinetic-rather than transport-limited because the system is open rather than closed with respect to oxygen. For example, studies investigating pyrite oxidation in mine tailings have documented that oxidation is limited by reaction kinetics (Elberling et al., 1994). In effect, as the transport of O_2 changes from advection of oxygenated water to depth in small watersheds to transport of air to mining-exposed pyrite in large watersheds, the overall rate-limiting step changes from transport-to kinetic-limited.

To test this hypothesis, we used a geospatial data set of coalbed lithology (East, 2013; Figure S2a in Supporting Information S1) and classified each watershed as “coal containing” (>0% of watershed area occupied by coal mining) or “non-coal containing” (0% coal mining). Using these classifications, we discovered that watersheds with coal show $C_{\text{sulf}}^{\text{max,obs}} > C_{\text{sulf}}^{\text{max,pred}}$, and those without show $C_{\text{sulf}}^{\text{max,obs}} < C_{\text{sulf}}^{\text{max,pred}}$ (Figure S3a in Supporting Information S1). We quantified this further by utilizing a logistic regression model. Logistic regression models work by fitting explanatory variables (i.e., drainage area) to binary responses (i.e., a watershed contains coal or does not). The model is fully described in Supporting Information S1. We analyzed 335 watersheds within the SRB and found that any watershed >1,355 km² has >50% chance of containing coalbeds. We conclude that in the SRB, stream chemistry yields evidence for a change in rate-limiting step at larger spatial scales (or a change from closed to open system with respect to oxygen), and this is likely because larger subbasins within the SRB always contain coal.

One issue in the SRB, however, is that spatial scale and coal-containing lithology co-vary; therefore, we cannot entirely disentangle the effects of coal mining from spatial scale. Thus, an alternate hypothesis might be that $C_{\text{sulf}}^{\text{max,obs}}$ increases above $C_{\text{sulf}}^{\text{max,pred}}$ simply because the watersheds are larger. As a first test of the scaling hypothesis, we identified two additional sites slightly north of the SRB that are large and contain no coal: the Hudson (USGS site 01358000; drainage area: 20,981 km²) and the Mohawk Rivers (USGS site 01357500; drainage area: 8,950 km²). Water quality data were accessed as for the SRB (see materials and methods). $C_{\text{sulf}}^{\text{max,obs}}$ values for these two watersheds equal 97 and 108 μM, respectively. These values are both below $C_{\text{sulf}}^{\text{max,pred}}$. This suggests that coal is a better explanation than watershed size for why $C_{\text{sulf}}^{\text{max,obs}} > C_{\text{sulf}}^{\text{max,pred}}$ in large subwatersheds of the SRB.

These arguments are consistent with a change in rate-limiting step (and a change from closed to open system with respect to oxygen) as watersheds become large enough to be coal-containing. In the next two sections, we provide additional evidence for the presence of coal mining in watersheds as the important variable (rather than scaling). First, we look at the power-law exponent in C - q behavior, and then we look at watersheds in other parts of the US. This latter investigation also allows us to determine if the behavior we document in the SRB is particular to just this one region or is more general.

4.4.2. Sulfate Concentration-Discharge Relationship

Many researchers have documented a power-law relationship between stream concentration, C , and discharge, q (Godsey et al., 2009) and have interpreted the power law exponent, b , in terms of physical processes:

$$C = aq^b \quad (13)$$

In addition to increases in $C_{\text{sulf}}^{\text{max,obs}}$, we therefore tested how coal mining impacts the power-law relationship between sulfate concentration and discharge. If DO is the sole oxidant source within a relatively closed system, then there is a fixed amount of oxidant available within any packet of water (i.e., the amount of O_2 that can be dissolved in water). In such systems where the source of the oxygen is dissolved in groundwater, we might expect C - q behavior is either chemostatic or dilution (i.e., $b \approx 0$ or $b < 0$) depending on whether dilution is fast enough to outcompete the rate of oxidation (i.e., transport or kinetic-limited, respectively). In contrast, if gaseous O_2 is freely accessing the pyrite-water interface because the system becomes open to the atmosphere, we might only expect dilution behavior (i.e., $b < 0$) because in such systems, oxidation is usually kinetic-limited (Elberling et al., 1994). We tested this using 92 watersheds throughout the SRB. For these sites, we did not separate the sources using our machine learning model due to limited concentration data availability, but rather calculated the C - q power law slope for total sulfate concentrations. We found that 71% of coal-containing watersheds show weak dilution C - q behavior ($b = -0.2 \pm 0.2$, $n = 56$), and 72% of non-coal containing watersheds show chemostatic C - q behavior ($b = 0.0 \pm 0.1$, $n = 36$; Figure S3b in Supporting Information S1). This supports our hypothesis of a change in rate-limiting step of pyrite reaction as a result of coal mining. Additionally, corroborating this conclusion, we also observed an inverse relationship between Dw and b in watersheds where both quantities were calculated (see Ibarra et al., 2016).

4.4.3. Other Systems With $C_{\text{sulf}}^{\text{max,obs}} > C_{\text{sulf}}^{\text{max,pred}}$

Although $C_{\text{sulf}}^{\text{max,obs}} > C_{\text{sulf}}^{\text{max,pred}}$ seems to be related to coal mining in the SRB, other systems with very high C_{sulf} have been reported globally. For example, C_{sulf} in rivers in Taiwan (Das et al., 2012), the Himalayas (Turchyn et al., 2013; Wolff-Boenisch et al., 2009), the Andes (Torres et al., 2016), Colorado (Winnick et al., 2017), and China (Liu et al., 2022) all exceed $188 \mu\text{M}$ (our assumed $C_{\text{sulf}}^{\text{max,pred}}$ based on a closed system where water was pre-equilibrated with the atmosphere). Like our hypotheses in Section 4.4.1, the authors have suggested several reasons for these high concentrations. Similar to our coal mining explanation, erosion rates in some of these mountainous watersheds could be high, leading to pyrite being shallow in the subsurface and exposed to soil or atmospheric gases. Winnick et al. (2017) hypothesize that the water table might seasonally fluctuate above and below the reaction front, exposing pyrite at low flow.

Our preferred explanation based on analysis in the SRB and other sites globally is that there are several circumstances where closed system dynamics might not accurately describe pyrite oxidation in watersheds, and these circumstances are likely related to enhanced exposure of pyrite to atmospheric gases (either natural through erosion or anthropogenic through mining). Gu, Rempe, et al. (2020) discuss how long-term pyrite oxidation rates are paced by erosion rates and hypothesizes that the mechanism by which erosion accelerates oxidation is that erosion accelerates fracturing, which in turn allows access of oxygen to more pyrite. In fact, pyrite is oxidized only around a few very deep fractures at Shale Hills but is more completely oxidized near the high densities of fractures created in other watersheds experiencing faster erosion (Gu, Heaney, et al., 2020). These long-term dependencies could lead to the variability we observe in the short-term oxidation dynamics. In other words, systems with high erosion rates such as Taiwan might be characterized by open-system oxidation dynamics over interannual timescales because of the high density of erosion-related fractures, whereas systems with low erosion rates such as Shale Hills might be characterized by closed-system oxidation dynamics over interannual timescales. This needs to be more thoroughly tested and provides a future avenue for research.

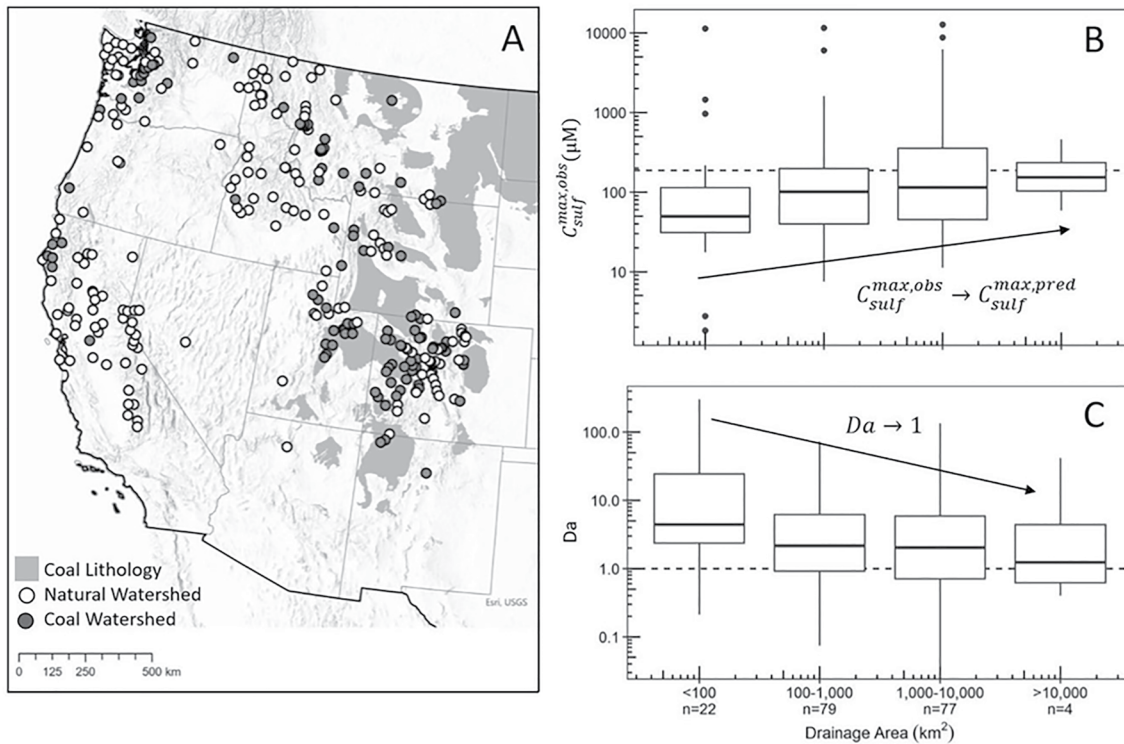


Figure 7. (a) Map showing the selected sites in the Western United States. Boxplots for natural (i.e., contains no coal) watersheds showing how (b) $C_{sulf}^{max,obs}$ and (c) Da change as a function of the drainage area of the watershed.

4.5. Application to Other Data Sets

To further investigate the effects of coal and watershed size on pyrite oxidation at the same time as exploring new climate and lithologic effects, we queried data within the WQP for the western US. In this region, we were able to investigate large watersheds on several lithologies in different climate regimes that do not contain coal. We identified 293 watersheds that fulfill the criteria outlined in materials and methods (109 with and 184 without coal-lithology; Figure 7a). Using this data set, we were able to test how pyrite oxidation changes as a function of drainage area of a watershed regardless of whether it contained coal. Using the total sulfate concentration and discharge, we calculated Dw and C_{sulf}^{max} for each watershed as described above (Equation 10).

Analogous to the eastern US results (i.e., SRB), watersheds with coal show $C_{sulf}^{max,obs} > C_{sulf}^{max,pred}$ and watersheds without coal tend to show $C_{sulf}^{max,obs} < C_{sulf}^{max,pred}$ (Figure S4 in Supporting Information S1). In addition, for watersheds without coal, as spatial scale increases, $C_{sulf}^{max,obs}$ approaches $C_{sulf}^{max,pred}$ ($=188 \mu\text{M}$) (Figure 7b) rather than increasing above $C_{sulf}^{max,pred}$ as observed in the SRB. Once again, this corroborates the findings from the SRB that $C_{sulf}^{max,obs} > C_{sulf}^{max,pred}$ is only observed in the presence of coal.

To explain why $C_{sulf}^{max,obs}$ approaches $C_{sulf}^{max,pred}$ ($=188 \mu\text{M}$) in the western data set, we turn back to observations at Shale Hills and Shaver's Creek. Explanations might include that the predominant flow path type changes and/or that the depth of the oxidation front changes relative to land surface as a function of spatial scale. In small headwater watersheds (like Shale Hills) flow paths above and within the pyrite reaction front contribute dominantly to the stream. In other words, the reaction front is relatively deep (Figure 2b), consistent with $C_{sulf}^{max,obs} < C_{sulf}^{max,pred}$ (Figure 8). In larger watersheds, flow paths through the pyrite reaction front are dominant, as evidenced by $C_{sulf}^{max,obs} = C_{sulf}^{max,pred}$. In addition, if watersheds are like Shaver's Creek, the pyrite reaction front is likely to become increasingly shallow as the stream incises into bedrock (Figure 2b), leading to $C_{sulf}^{max,obs} = C_{sulf}^{max,pred}$ (Figure 8).

In addition to $C_{sulf}^{max,obs}$, we found that Dw (and Da) also change with scale. In particular, as watersheds get larger, Da approaches 1. In relationship to Equation 4, this can be conceptualized as l approaches L as watersheds get larger.

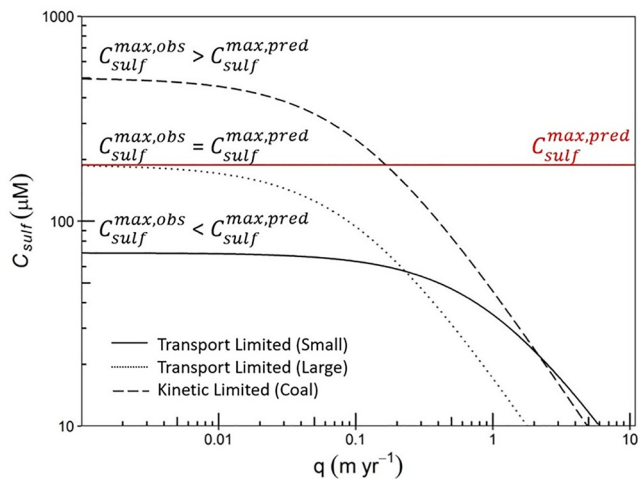


Figure 8. Schematic plot showing the three characteristic concentration-discharge patterns observed in watersheds in the northeastern and western US. By studying catchments within the Susquehanna River Basin and western US, we observed that pyrite oxidation is always limited by advective transport of the oxidant to the mineral everywhere except where coal has been exhumed at the land surface. For the latter catchments, oxidation is kinetic- (or reaction-) limited. In this plot, $C_{sulf}^{max,obs}$ equals 500, 188, and 70 μM for the kinetic-limited, transport-limited (large), and transport-limited (small) curves, respectively. Dw is 1 for transport limited (small) and 0.1 for kinetic limited and transport limited (large).

4.6. Subsurface Redox Architecture in Small and Large Watersheds

To recap the observations, as watersheds without coal become larger, we found that $C_{sulf}^{max,obs}$ approaches $C_{sulf}^{max,pred}$ and Da approaches 1 (Figure 7). Both observations are consistent with l approaching L (see Equation 12). We propose two ways to interpret this observation for these United States data. The first explanation is that as watersheds get larger, their streams integrate water from deeper flow paths where water is more likely to have traveled completely through the reaction front, depleting DO completely (i.e., flow path 3; Figure 2b). The second explanation is that streams incise into the pyrite reaction zones in increasingly larger watersheds. It is important to note that these two explanations are not mutually exclusive. For example, deeper flow paths might be depleted with respect to DO, resulting in a shallowing of the reaction front.

Explanation 1 implies that flow length and depth of flow both increase as drainage area increases. This idea is a corollary to hydrologic models which show only local flow paths contributing to flow in first order streams but significant regional groundwater flow paths contributing to third order streams (Gleeson & Manning, 2008). However, tributaries also enter the mainstem of large rivers contributing significantly to streamflow. Instead of integrating deeper flow paths, therefore, large rivers might simply be manifesting the influence of their tributaries (i.e., higher order streams are a summation of lower order streams; Hrachowitz et al., 2010; Shaman et al., 2004). For example, runoff in watersheds in the Neversink River watershed in New York changed little between subcatchments exceeding 21 km^2 (Shaman et al., 2004). This suggests that water from deeper flow paths only

significantly increase streamflow in moderately small watersheds. Moreover, in another study, mean transit times of water in streams converged to the same value at increasingly large watershed scale, and large watersheds showed no major change of dominant flow paths (Hrachowitz et al., 2010). Given these findings, variations in flow length and depth likely describe some of the differences between small in large watersheds, but they cannot solely account for all the trends in our data.

We, therefore, favor explanation two: reaction fronts shallow as watershed size increases. Instead of flow paths becoming consistently deeper, allowing stream waters to have interacted with pyrite for longer, the reaction front instead shallows such that shallow flow paths are within the reaction front rather than above it (i.e., flow path type 1 disappears in favor of flow path type 2; Figure 2b). This explanation is also consistent with the observation of unoxidized pyrite outcropping along sections of Shaver's Creek (Figure S1 in Supporting Information S1) and in other locations such as northern California and Taiwan (Gu, Rempe, et al., 2020). Headwater streams (i.e., zeroth or first order) may generally develop deep pyrite oxidation fronts at least partly because recharging water has high concentrations of DO. But as groundwater flows from the headwaters downstream to join higher-order streams, it becomes depleted with respect to DO and in turn becomes less reactive with pyrite; therefore, the reaction front shallows downstream (schematically depicted in Figure 2b). Because the reaction front is less deep downstream, shallower flow paths interact with pyrite leading to increased $C_{sulf}^{max,obs}$. This interpretation of our data thus emphasizes changes in the subsurface redox architecture as a function of watershed size. Integrating subsurface mineral distributions into conceptual and hydrologic models will help improve water quality predictions.

5. Conclusions

Through a combination of machine learning and physically based modeling, we investigated the mechanism of pyrite oxidation recorded in the concentration-discharge relationships of streams. We found three characteristic concentration-discharge trends as depicted in Figure 8. In small watersheds without coal, we found that the maximum stream sulfate concentrations are less than predicted by equilibrium with pyrite ($C_{sulf}^{max,obs} < C_{sulf}^{max,pred}$), and the Damköhler number (Da) is greater than 1. In large watersheds without coal $C_{sulf}^{max,obs} = C_{sulf}^{max,pred}$ and $Da = 1$. We attribute this partly to subsurface flow paths that get deeper and longer as spatial scale increases but also, more importantly, to downstream shallowing of the pyrite reaction front in larger watersheds. Nonetheless, across

all spatial scales, the advective transport of DO to the reaction front limits pyrite oxidation in these watersheds (Figure 8).

On the other hand, coal mining results in $C_{\text{sulf}}^{\text{max,obs}} > C_{\text{sulf}}^{\text{max,pred}}$ across all-sized watersheds, which is consistent with kinetic-limited, rather than transport-limited, oxidation of exhumed pyrite (Figure 8). We attribute the effect of mining to the enhanced exposure of pyrite to atmospheric oxygen which allows open-system rather than closed-system oxidation, a transition that might also occur with increasing fracture density in high erosion rate watersheds. We also found that coal containing watersheds have steeper C - q power law slopes (i.e., more negative b values) than non-coal containing watersheds; therefore, C - q slopes might indicate the relative importance of kinetic-versus transport-limited oxidation. Through analysis of C - q relationships, we were able to determine information about subsurface flow paths, the subsurface redox architecture, and oxidant source dynamics, all of which will help to elucidate reaction mechanisms across spatial scales. Understanding the subsurface redox architecture of a watershed will help to improve our predictions of legacy contamination in the future.

Conflict of Interest

The authors declare no conflicts of interest relevant to this study.

Data Availability Statement

All data are available in the main text, in Supporting Information S1, published on the SSHCZO Website (http://www.czo.psu.edu/data_geochemical_geophysical.html), or accessible via the water quality portal (<https://www.waterqualitydata.us/>). For ease of use, we have aggregated these data sets, as well as the codes used in the NMF modeling, which can be found on GitHub (<https://github.com/shaughnessyar/NMF>; Shaughnessy, 2023).

Acknowledgments

This research was partly conducted in Penn State's Stone Valley Forest, which is funded by the Penn State College of Agriculture Sciences, Department of Ecosystem Science and Management, and managed by the staff of the Forestlands Management Office as well as Brandon Forsythe, who is acknowledged for field help and interpretations. Chemical analyses were conducted at Penn State's Laboratory for Isotopes and Metals in the Environment (LIME). Solid phases were characterized at Penn State's Materials Characteristics Laboratory (MCL). Oak Ridge National Laboratory (ORNL) is managed by UT-Battelle, LLC, under contract DE-AC05-00OR22725 with the U.S. DOE.

References

- Alewell, C., Mitchell, M., & Likens, G. (1919). *Sulfate isotopes in precipitation and stream water* (pp. 1966–1994). Hubbard Brook Experimental Forest.
- Berner, R. A. (1978). Rate control of mineral dissolution under Earth surface conditions. *American Journal of Science*, 278(9), 1235–1252. <https://doi.org/10.2475/ajs.278.9.1235>
- Birkel, C., Soulsby, C., & Tetzlaff, D. (2011). Modeling catchment-scale water storage dynamics: Reconciling dynamic storage with tracer-inferred passive storage. *Hydrological Processes*, 25, 3924–3936. <https://doi.org/10.1002/hyp.8201>
- Bochet, O., Bethencourt, L., Dufresne, A., Farasin, J., Pédrot, M., Labasque, T., et al. (2020). Iron-oxidizer hotspots formed by intermittent oxic-anoxic fluid mixing in fractured rocks. *Nature Geoscience*, 13(2), 149–155. <https://doi.org/10.1038/s41561-019-0509-1>
- Bolton, E. W., Berner, R. A., & Petsch, S. T. (2006). The weathering of sedimentary organic matter as a control on atmospheric O₂: II. Theoretical modeling. *American Journal of Science*, 306(8), 575–615. <https://doi.org/10.2475/08.2006.01>
- Borch, T., Kretzschmar, R., Kappler, A., Cappellen, P. V., Ginder-Vogel, M., Voegelin, A., & Campbell, K. (2010). Biogeochemical redox processes and their impact on contaminant dynamics. *Environmental Science & Technology*, 44(1), 15–23. <https://doi.org/10.1021/es9026248>
- Brantley, S. L., Bazilevskaya, E., Andrews, D., Williams, J. Z., Herndon, E., Holmes, G., et al. (2013a). Susquehanna Shale Hills Critical Zone Observatory stream water chemistry (2010). *Interdisciplinary Earth Data Alliance (IEDA), EarthChem*. <https://doi.org/10.1594/IEDA/100243>
- Brantley, S. L., Fisher, J., Neal, A., Russo, T., Sullivan, P. L., Cain, M., & Hoagland, B. (2018a). Susquehanna Shale Hills Critical Zone Observatory—Shaver's Creek watershed stream chemistry (2014). *Interdisciplinary Earth Data Alliance (IEDA)*. <https://doi.org/10.1594/IEDA/100611>
- Brantley, S. L., Forsythe, B., Hoagland, B., Pederson, D., & Russo, T. (2018). Susquehanna Shale Hills Critical Zone Observatory—Shaver's Creek watershed stream chemistry (2015). *Interdisciplinary Earth Data Alliance (IEDA)*. <https://doi.org/10.1594/IEDA/100612>
- Brantley, S. L., Holleran, M. E., Jin, L., & Bazilevskaya, E. (2014). Probing deep weathering in the Shale Hills Critical Zone Observatory, Pennsylvania (USA): The hypothesis of nested chemical reaction fronts in the subsurface. *Earth Surface Processes and Landforms*, 38(11), 1280–1298. <https://doi.org/10.1002/esp.3415>
- Brantley, S. L., Jin, L., Andrews, D., Holmes, G., Bhatt, M., Holleran, M., et al. (2013b). Susquehanna Shale Hills Critical Zone Observatory stream water chemistry (2009). *Interdisciplinary Earth Data Alliance (IEDA), EarthChem*. <https://doi.org/10.1594/IEDA/100242>
- Brantley, S. L., Jin, L., Andrews, D., Holmes, G., Holleran, M., Williams, J. Z., et al. (2013c). Susquehanna Shale Hills Critical Zone Observatory stream water chemistry (2008). *Interdisciplinary Earth Data Alliance (IEDA), EarthChem*. <https://doi.org/10.1594/IEDA/100241>
- Brantley, S. L., & Lebedeva, M. I. (2021). Relating land surface, water table, and weathering fronts with a conceptual valve model for headwater catchments. *Hydrological Processes*, 35(2), e14010. <https://doi.org/10.1002/hyp.14010>
- Brantley, S. L., White, T., West, N., Williams, J. Z., Forsythe, B., Shapich, D., et al. (2018b). Susquehanna Shale Hills Critical Zone Observatory: Shale hills in the context of Shaver's Creek watershed. *Vadose Zone Journal*, 17(1), 1–19. <https://doi.org/10.2136/vzj2018.04.0092>
- Calmels, D., Gaillardet, J., Brenot, A., & France-Lanord, C. (2007). Sustained sulfide oxidation by physical erosion processes in the Mackenzie River basin: Climatic perspectives. *Geology*, 35(11), 1003–1006. <https://doi.org/10.1130/g24132a.1>
- Christophersen, N., & Hooper, R. P. (1992). Multivariate analysis of stream water chemical data: The use of principal components analysis for the end-member mixing problem. *Water Resources Research*, 28(1), 99–107. <https://doi.org/10.1029/91wr02518>
- Close, M. E., Abraham, P., Humphries, B., Lilburne, L., Cuthill, T., & Wilson, S. (2016). Predicting groundwater redox status on a regional scale using linear discriminant analysis. *Journal of Contaminant Hydrology*, 191, 19–32. <https://doi.org/10.1016/j.jconhyd.2016.04.006>

- Cole, T. L., Torres, M. A., & Kemeny, P. C. (2022). The hydrochemical signature of incongruent weathering in Iceland. *Journal of Geophysical Research: Earth Surface*, 127(6), e2021JF006450. <https://doi.org/10.1029/2021j006450>
- Das, A., Chung, C. H., & You, C. F. (2012). Disproportionately high rates of sulfide oxidation from mountainous river basins of Taiwan orogeny: Sulfur isotope evidence. *Geophysical Research Letters*, 39(12). <https://doi.org/10.1029/2012gl015149>
- De Cicco, L. A., Hirsch, R. M., Lorenz, D., & Watkins, W. D. (2018). dataRetrieval: R packages for discovering and retrieving water data available from Federal hydrologic web services. <https://doi.org/10.5066/P9X4L3GE>
- East, J. A. (2013). *Coal fields of the conterminous United States—National Coal Resource Assessment updated version (No. 2012-1205)*. US Geological Survey.
- Elberling, B., Nicholson, R. V., & Scharer, J. M. (1994). A combined kinetic and diffusion model for pyrite oxidation in tailings: A change in controls with time. *Journal of Hydrology*, 157(1–4), 47–60. [https://doi.org/10.1016/0022-1694\(94\)90098-1](https://doi.org/10.1016/0022-1694(94)90098-1)
- Epuna, F., Shaheen, S. W., & Wen, T. (2022). Road salting and natural brine migration revealed as major sources of groundwater contamination across regions of northern Appalachia with and without unconventional oil and gas development. *Water Research*, 225, 119128. <https://doi.org/10.1016/j.watres.2022.119128>
- Essaid, H. I., Bekins, B. A., & Cozzarelli, I. M. (2015). Organic contaminant transport and fate in the subsurface: Evolution of knowledge and understanding. *Water Resources Research*, 51(7), 4861–4902. <https://doi.org/10.1002/2015wr017121>
- Forgeng, M. (2021). Investigating nitrate transport and denitrification in hilly terrain from the scale of a single farm field to a HUC-10 watershed (Masters thesis). Pennsylvania State University.
- Friedel, M. J., Wilson, S. R., Close, M. E., Buscema, M., Abraham, P., & Banasiak, L. (2020). Comparison of four learning-based methods for predicting groundwater redox status. *Journal of Hydrology*, 580, 124200. <https://doi.org/10.1016/j.jhydrol.2019.124200>
- Fry, B., Silva, S. R., Kendall, C., & Anderson, R. K. (2002). Oxygen isotope corrections for online $\delta^{34}\text{S}$ analysis. *Rapid Communications in Mass Spectrometry*, 16(9), 854–858. <https://doi.org/10.1002/rcm.651>
- Gaillardet, J., Dupré, B., Louvat, P., & Allegre, C. J. (1999). Global silicate weathering and CO_2 consumption rates deduced from the chemistry of large rivers. *Chemical Geology*, 159(1–4), 3–30. [https://doi.org/10.1016/s0009-2541\(99\)00031-5](https://doi.org/10.1016/s0009-2541(99)00031-5)
- Galaviz-Villa, I., Landeros-Sánchez, C., del Refugio Castañeda-Chávez, M., Martínez-Dávila, J. P., Pérez-Vázquez, A., Nikolskii-Gavrilov, I., & Lango-Reynoso, F. (2010). Agricultural contamination of subterranean water with nitrates and nitrites: An environmental and public health problem. *Journal of Agricultural Science*, 2(2), 17.
- Gleeson, T., & Manning, A. H. (2008). Regional groundwater flow in mountainous terrain: Three-dimensional simulations of topographic and hydrogeologic controls. *Water Resources Research*, 44(10). <https://doi.org/10.1029/2008wr006848>
- Godsey, S. E., Kirchner, J. W., & Clow, D. W. (2009). Concentration-discharge relationships reflect chemostatic characteristics of US catchments. *Hydrological Processes: International Journal*, 23(13), 1844–1864. <https://doi.org/10.1002/hyp.7315>
- Grothendieck, G. (2013). Nonlinear regression with brute force. *R package version 0.2*.
- Gu, X., Heaney, P. J., Reis, F. D. A., & Brantley, S. L. (2020). Deep abiotic weathering of pyrite. *Science*, 370(6515), eabb8092. <https://doi.org/10.1126/science.abb8092>
- Gu, X., Mavko, G., Ma, L., Oakley, D., Accardo, N., Carr, B. J., et al. (2020). Seismic refraction tracks porosity generation and possible CO_2 production at depth under a headwater catchment. *Proceedings of the National Academy of Sciences*, 117(32), 18991–18997. <https://doi.org/10.1073/pnas.2003451117>
- Gu, X., Rempe, D. M., Dietrich, W. E., West, A. J., Lin, T. C., Jin, L., & Brantley, S. L. (2020). Chemical reactions, porosity, and microfracturing in shale during weathering: The effect of erosion rate. *Geochimica et Cosmochimica Acta*, 269, 63–100. <https://doi.org/10.1016/j.gca.2019.09.044>
- Hartmann, J. (2009). Bicarbonate-fluxes and CO_2 -consumption by chemical weathering on the Japanese Archipelago—Application of a multi-lithological model framework. *Chemical Geology*, 265(3–4), 237–271. <https://doi.org/10.1016/j.chemgeo.2009.03.024>
- Hemingway, J. D., Hilton, R. G., Hovius, N., Eglinton, T. I., Haghipour, N., Wacker, L., et al. (2018). Microbial oxidation of lithospheric organic carbon in rapidly eroding tropical mountain soils. *Science*, 360(6385), 209–212. <https://doi.org/10.1126/science.aao6463>
- Hilton, R. G., Turowski, J. M., Winnick, M., Dellinger, M., Schleppli, P., Williams, K. H., et al. (2021). Concentration-discharge relationships of dissolved rhenium in Alpine catchments reveal its use as a tracer of oxidative weathering. *Water Resources Research*, 57(11), e2021WR029844. <https://doi.org/10.1029/2021wr029844>
- Hoagland, B., Russo, T. A., Gu, X., Hill, L., Kaye, J., Forsythe, B., & Brantley, S. L. (2017). Hyporheic zone influences on concentration-discharge relationships in a headwater sandstone stream. *Water Resources Research*, 53(6), 4643–4667. <https://doi.org/10.1002/2016wr019717>
- Hodges, C., Kim, H., Brantley, S. L., & Kaye, J. (2019). Soil CO_2 and O_2 concentrations illuminate the relative importance of weathering and respiration to seasonal soil gas fluctuations. *Soil Science Society of America Journal*, 83(4), 1167–1180. <https://doi.org/10.2136/sssaj2019.02.0049>
- Hrachowitz, M., Soulsby, C., Tetzlaff, D., & Speed, M. (2010). Catchment transit times and landscape controls—Does scale matter? *Hydrological Processes: International Journal*, 24(1), 117–125. <https://doi.org/10.1002/hyp.7510>
- Ibarra, D. E., Caves, J. K., Moon, S., Thomas, D. L., Hartmann, J., Chamberlain, C. P., & Maher, K. (2016). Differential weathering of basaltic and granitic catchments from concentration-discharge relationships. *Geochimica et Cosmochimica Acta*, 190, 265–293. <https://doi.org/10.1016/j.gca.2016.07.006>
- Ibarra, D. E., Moon, S., Caves, J. K., Chamberlain, C. P., & Maher, K. (2017). Concentration-discharge patterns of weathering products from global rivers. *Acta Geochimica*, 36(3), 405–409. <https://doi.org/10.1007/s11631-017-0177-z>
- Jin, L., Ogrinc, N., Yesavage, T., Hasenmueller, E. A., Ma, L., Sullivan, P. L., et al. (2014). The CO_2 consumption potential during gray shale weathering: Insights from the evolution of carbon isotopes in the Susquehanna Shale Hills Critical Zone Observatory. *Geochimica et Cosmochimica Acta*, 142, 260–280. <https://doi.org/10.1016/j.gca.2014.07.006>
- Johnson, A. C., Romaniello, S. J., Reinhard, C. T., Gregory, D. D., Garcia-Robledo, E., Revsbech, N. P., et al. (2019). Experimental determination of pyrite and molybdenite oxidation kinetics at nanomolar oxygen concentrations. *Geochimica et Cosmochimica Acta*, 249, 160–172. <https://doi.org/10.1016/j.gca.2019.01.022>
- Juncher Jørgensen, C., Jacobsen, O. S., Elberling, B., & Aamand, J. (2009). Microbial oxidation of pyrite coupled to nitrate reduction in anoxic groundwater sediment. *Environmental Science & Technology*, 43(13), 4851–4857.
- Kemeny, P. C., Lopez, G. I., Dalleska, N. F., Torres, M., Burke, A., Bhatt, M. P., et al. (2021). Sulfate sulfur isotopes and major ion chemistry reveal that pyrite oxidation counteracts CO_2 drawdown from silicate weathering in the Langtang-Trisuli-Narayani River system, Nepal Himalaya. *Geochimica et Cosmochimica Acta*, 294, 43–69. <https://doi.org/10.1016/j.gca.2020.11.009>
- Kemeny, P. C., & Torres, M. A. (2021). Presentation and applications of mixing elements and dissolved isotopes in rivers (MEANDIR), a customizable MATLAB model for Monte Carlo inversion of dissolved river chemistry. *American Journal of Science*, 321(5), 579–642. <https://doi.org/10.2475/05.2021.03>

- Kim, H., Høyer, A. S., Jakobsen, R., Thorling, L., Aamand, J., Maurya, P. K., et al. (2019). 3D characterization of the subsurface redox architecture in complex geological settings. *Science of the Total Environment*, 693, 133583. <https://doi.org/10.1016/j.scitotenv.2019.133583>
- Kirchner, J. W. (2009). Catchments as simple dynamical systems: Catchment characterization, rainfall-runoff modeling, and doing hydrology backward. *Water Resources Research*, 45(2). <https://doi.org/10.1029/2008wr006912>
- Kump, L. R., Brantley, S. L., & Arthur, M. A. (2000). Chemical weathering, atmospheric CO₂ and climate. *Annual Reviews of Earth and Planetary Sciences*, 28(1), 611–667. <https://doi.org/10.1146/annurev.earth.28.1.611>
- Le Gendre, E., Martin, E., Villemant, B., Cartigny, P., & Assayag, N. (2017). A simple and reliable anion-exchange resin method for sulfate extraction and purification suitable for multiple O-and S-isotope measurements. *Rapid Communications in Mass Spectrometry*, 31(1), 137–144. <https://doi.org/10.1002/rcm.7771>
- Liao, R., Gu, X., & Brantley, S. L. (2022). Weathering of chlorite from grain to watershed: The role and distribution of oxidation reactions in the subsurface. *Geochimica et Cosmochimica Acta*, 333, 284–307. <https://doi.org/10.1016/j.gca.2022.07.019>
- Liu, J., Han, G., Zhang, Q., Liu, M., & Li, X. (2022). Stable isotopes and Bayesian tracer mixing model reveal chemical weathering and CO₂ release in the Jiulongjiang River basin, Southeast China. *Water Resources Research*, 58(9), e2021WR031738. <https://doi.org/10.1029/2021wr031738>
- Maher, K., & Chamberlain, C. P. (2014). Hydrologic regulation of chemical weathering and the geologic carbon cycle. *Science*, 343(6178), 1502–1504. <https://doi.org/10.1126/science.1250770>
- Meybeck, M. (1987). Global chemical weathering of surficial rocks estimated from river dissolved loads. *American Journal of Science*, 287(5), 401–428. <https://doi.org/10.2475/ajs.287.5.401>
- Möller, D. (1990). The Na/Cl ratio in rainwater and the sea-salt chloride cycle. *Tellus B: Chemical and Physical Meteorology*, 42(3), 254–262. <https://doi.org/10.1034/j.1600-0889.1990.t01-1-00004.x>
- Molli, G., Doveri, M., Manzella, A., Bonini, L., Botti, F., Menichini, M., et al. (2015). Surface-subsurface structural architecture and groundwater flow of the Equi Terme hydrothermal area, northern Tuscany Italy. *Italian Journal of Geosciences*, 134(3), 442–457. <https://doi.org/10.3301/ijg.2014.25>
- Neal, C., & Kirchner, J. W. (2000). Sodium and chloride levels in rainfall, mist, stream water, and groundwater at the Plynlion catchments, mid-Wales: Inferences on hydrological and chemical controls. *Hydrology and Earth System Sciences*, 4(2), 295–310. <https://doi.org/10.5194/hess-4-295-2000>
- Ogrič, M., Dellinger, M., Grant, K. E., Galy, V., Gu, X., Brantley, S. L., & Hilton, R. G. (2023). Low rates of rock organic carbon oxidation and anthropogenic cycling of rhenium in a slowly denuding landscape. *Earth Surface Processes and Landforms*.
- Petsch, S. T., Berner, R. A., & Eglinton, T. I. (2000). A field study of the chemical weathering of ancient sedimentary organic matter. *Organic Geochemistry*, 31(5), 475–487. [https://doi.org/10.1016/s0146-6380\(00\)00014-0](https://doi.org/10.1016/s0146-6380(00)00014-0)
- Poole, G. C., Stanford, J. A., Running, S. W., & Frissell, C. A. (2006). Multiscale geomorphic drivers of groundwater flow paths: Subsurface hydrologic dynamics and hyporheic habitat diversity. *Journal of the North American Benthological Society*, 25(2), 288–303. [https://doi.org/10.1899/0887-3593\(2006\)25\[288:mgdogf\]2.0.co;2](https://doi.org/10.1899/0887-3593(2006)25[288:mgdogf]2.0.co;2)
- Raymond, P. A., & Oh, N. H. (2009). Long-term changes of chemical weathering products in rivers heavily impacted from acid mine drainage: Insights on the impact of coal mining on regional and global carbon and sulfur budgets. *Earth and Planetary Science Letters*, 284(1–2), 50–56. <https://doi.org/10.1016/j.epsl.2009.04.006>
- Read, E. K., Carr, L., De Cicco, L., Dugan, H. A., Hanson, P. C., Hart, J. A., et al. (2017). Water quality data for national-scale aquatic research: The Water Quality Portal. *Water Resources Research*, 53(2), 1735–1745. <https://doi.org/10.1002/2016wr019993>
- Shaheen, S. W., Wen, T., Herman, A., & Brantley, S. L. (2022). Geochemical evidence of potential groundwater contamination with human health risks where hydraulic fracturing overlaps with extensive legacy hydrocarbon extraction. *Environmental Science & Technology*, 56(14), 10010–10019. <https://doi.org/10.1021/acs.est.2c00001>
- Shaman, J., Stieglitz, M., & Burns, D. (2004). Are big basins just the sum of small catchments? *Hydrological Processes*, 18(16), 3195–3206. <https://doi.org/10.1002/hyp.5739>
- Shaughnessy, A. R. (2023). [Dataset], [Software] shaughnessyar/NMF: NMF Codes for the Susquehanna River Basin (v0.1.0). Zenodo. <https://doi.org/10.5281/zenodo.7558750>
- Shaughnessy, A. R., Gu, X., Wen, T., & Brantley, S. L. (2021). Machine learning deciphers CO₂ sequestration and subsurface flow paths from stream chemistry. *Hydrology and Earth System Sciences*, 25(6), 3397–3409. <https://doi.org/10.5194/hess-25-3397-2021>
- Silverman, M. P. (1967). Mechanism of bacterial pyrite oxidation. *Journal of Bacteriology*, 94(4), 1046–1051. <https://doi.org/10.1128/jb.94.4.1046-1051.1967>
- Sullivan, P. L., Hynke, S. A., Gu, X., Singha, K., White, T., West, N., et al. (2016). Oxidative dissolution under the channel leads geomorphological evolution at the Shale Hills catchment. *American Journal of Science*, 316(10), 981–1026. <https://doi.org/10.2475/10.2016.02>
- Tesoriero, A. J., Duff, J. H., Saad, D. A., Spahr, N. E., & Wolock, D. M. (2013). Vulnerability of streams to legacy nitrate sources. *Environmental Science & Technology*, 47(8), 3623–3629. <https://doi.org/10.1021/es305026x>
- Tesoriero, A. J., Gronberg, J. A., Juckem, P. F., Miller, M. P., & Austin, B. P. (2017). Predicting redox-sensitive contaminant concentrations in groundwater using random forest classification. *Water Resources Research*, 53(8), 7316–7331. <https://doi.org/10.1002/2016wr020197>
- Tesoriero, A. J., Terziotti, S., & Abrams, D. B. (2015). Predicting redox conditions in groundwater at a regional scale. *Environmental Science & Technology*, 49(16), 9657–9664. <https://doi.org/10.1021/acs.est.5b01869>
- Torrentó, C., Urmeneta, J., Otero, N., Soler, A., Viñas, M., & Cama, J. (2011). Enhanced denitrification in groundwater and sediments from a nitrate-contaminated aquifer after addition of pyrite. *Chemical Geology*, 287(1–2), 90–101. <https://doi.org/10.1016/j.chemgeo.2011.06.002>
- Torres, M. A., & Baronas, J. J. (2021). Modulation of riverine concentration-discharge relationships by changes in the shape of the water transit time distribution. *Global Biogeochemical Cycles*, 35(1), e2020GB006694. <https://doi.org/10.1029/2020gb006694>
- Torres, M. A., West, A. J., & Clark, K. E. (2015). Geomorphic regime modulates hydrologic control of chemical weathering in the Andes-Amazon. *Geochimica et Cosmochimica Acta*, 166, 105–128. <https://doi.org/10.1016/j.gca.2015.06.007>
- Torres, M. A., West, A. J., Clark, K. E., Paris, G., Bouchez, J., Ponton, C., et al. (2016). The acid and alkalinity budgets of weathering in the Andes-Amazon system: Insights into the erosional control of global biogeochemical cycles. *Earth and Planetary Science Letters*, 450, 381–391. <https://doi.org/10.1016/j.epsl.2016.06.012>
- Turchyn, A. V., Tipper, E. T., Galy, A., Lo, J. K., & Bickle, M. J. (2013). Isotope evidence for secondary sulfide precipitation along the Marsyandi River, Nepal, Himalayas. *Earth and Planetary Science Letters*, 374, 36–46. <https://doi.org/10.1016/j.epsl.2013.04.033>
- Van Meter, K. J., Basu, N. B., & Van Cappellen, P. (2017). Two centuries of nitrogen dynamics: Legacy sources and sinks in the Mississippi and Susquehanna River Basins. *Global Biogeochemical Cycles*, 31(1), 2–23. <https://doi.org/10.1002/2016gb005498>
- Van Meter, K. J., Van Cappellen, P., & Basu, N. B. (2018). Legacy nitrogen may prevent achievement of water quality goals in the Gulf of Mexico. *Science*, 360(6387), 427–430. <https://doi.org/10.1126/science.aar4462>

- Wan, J., Tokunaga, T. K., Williams, K. H., Dong, W., Brown, W., Henderson, A. N., et al. (2019). Predicting sedimentary bedrock subsurface weathering fronts and weathering rates. *Scientific Reports*, 9(1), 1–10. <https://doi.org/10.1038/s41598-019-53205-2>
- Winnick, M. J., Carroll, R. W., Williams, K. H., Maxwell, R. M., Dong, W., & Maher, K. (2017). Snowmelt controls on concentration-discharge relationships and the balance of oxidative and acid-base weathering fluxes in an alpine catchment, East River, Colorado. *Water Resources Research*, 53(3), 2507–2523. <https://doi.org/10.1002/2016wr019724>
- Wolff-Boenisch, D., Gabet, E. J., Burbank, D. W., Langner, H., & Putkonen, J. (2009). Spatial variations in chemical weathering and CO₂ consumption in Nepalese High Himalayan catchments during the monsoon season. *Geochimica et Cosmochimica Acta*, 73(11), 3148–3170. <https://doi.org/10.1016/j.gca.2009.03.012>
- Wymore, A. S., Brereton, R. L., Ibarra, D. E., Maher, K., & McDowell, W. H. (2017). Critical zone structure controls concentration-discharge relationships and solute generation in forested tropical montane watersheds. *Water Resources Research*, 53(7), 6279–6295. <https://doi.org/10.1002/2016wr020016>
- Xu, Z., Hariharan, J., Passalacqua, P., Steel, E., Chadwick, A., Paola, C., et al. (2022). Effects of geologic setting on contaminant transport in deltaic aquifers. *Water Resources Research*, 58(9), e2022WR031943. <https://doi.org/10.1029/2022wr031943>
- Xu, Z., Hariharan, J., Passalacqua, P., Steel, E., Paola, C., & Michael, H. A. (2021). Linking the surface and subsurface in river deltas—Part 2: Relating subsurface geometry to groundwater flow behavior. *Water Resources Research*, 57(8), e2020WR029281. <https://doi.org/10.1029/2020wr029281>
- Zhang, D., Li, X. D., Zhao, Z. Q., & Liu, C. Q. (2015). Using dual isotopic data to track the sources and behaviors of dissolved sulfate in the western North China Plain. *Applied Geochemistry*, 52, 43–56. <https://doi.org/10.1016/j.apgeochem.2014.11.011>
- Zhi, W., Li, L., Dong, W., Brown, W., Kaye, J., Steefel, C., & Williams, K. H. (2019). Distinct source water chemistry shapes contrasting concentration-discharge patterns. *Water Resources Research*, 55(5), 4233–4251. <https://doi.org/10.1029/2018wr024257>
- Zhong, J., Li, S. L., Ibarra, D. E., Ding, H., & Liu, C. Q. (2020). Solute production and transport processes in Chinese monsoonal rivers: Implications for global climate change. *Global Biogeochemical Cycles*, 34(9), e2020GB006541. <https://doi.org/10.1029/2020gb006541>